A numerical assessment of local strain measurements on the attenuation and modulus dispersion in rocks with fluid heterogeneities

Chao Sun, Genyan Tang, Samuel Chapman, Huai Zhang, Jérôme Fortin, Shangxu Wang, Dongming Pan, Jianhua Yue

Geophysical Journal International

Geophys. J. Int. (2023) **235,** 951–969
Advance Access publication 2023 July 14
GJI Rock and Mineral Physics, Rheology

https://doi.org/10.1093/gji/ggad289

A numerical assessment of local strain measurements on the attenuation and modulus dispersion in rocks with fluid heterogeneities

Chao Sun,[1] Genyan Tang,[2] Samuel Chapman,[3] Huai Zhang,[4,5,6] Jérôme Fortin,[3] Shangxu Wang,[2] Dongming Pan[1] and Jianhua Yue[1]

[1]*College of Resources and Geoscience, China University of Mining and Technology, XuZhou* 221116, *China E-mail: hzhang@ucas.ac.cn*
[2]*China University of Petroleum, Beijing. State Key Laboratory of Petroleum Resources and Prospecting; Key Laboratory of Geophysical Prospecting, CNPC, Changping, Beijing* 102249, *China*
[3]*Laboratoire de Géologie, Ecole Normale Supérieure/CNRS, UMR*8538, *PSL Research University,* 75005 *Paris, France*
[4]*Key Laboratory of Computational Geodynamics, Chinese Academy of Sciences, University of Chinese Academy of Sciences, Beijing* 100049, *China*
[5]*Southern Marine Science and Engineering Guangdong Laboratory (Zhuhai), Guangdong Zhuhai* 519080, *China*
[6]*Beijing Yanshan Earth Critical Zone National Research Station, University of Chinese Academy of Sciences, Beijing* 101408, *China*

Accepted 2023 July 12. Received 2023 June 16; in original form 2023 March 6

SUMMARY

The forced oscillation method is widely used to investigate intrinsic seismic wave dispersion and attenuation in rock samples by measuring their dynamic stress–strain response. However, using strain gauges to locally measure the strains on samples surfaces can result in errors in determining the attenuation and moduli of rocks with mesoscopic scale heterogeneities. In this study, we developed a 3-D numerical model based on Biot's poroelastic theory to investigate the effect of strain gauge location, number and size on attenuation and dispersion in response to wave-induced fluid flow. Our results show that increasing the strain gauge length, number, and size can reduce the error between local and bulk responses. In a homogeneous and isotropic rock with a quasi-fractal fluid heterogeneity at 12 per cent gas saturation, the relative error between local and bulk responses stays below 6 per cent when the strain gauge length surpasses 8.6 times the correlation length. As the gas saturation becomes larger, the ratio minimally changes non-monotonically, initially increasing and then decreasing. We also used the Monte Carlo method to demonstrate that local laboratory measurements can approximate the reservoir-scale response with a minimum relative error of 1.5 per cent as the sample number increases. Our findings provide guidance for (i) interpreting local low-frequency measurements in terms of bulk properties of rock and (ii) upscaling lab measurements to reservoir-scale properties.

Key words: Numerical modelling; Seismic attenuation; Mechanics, theory and modelling; Fluid heterogeneity; Dispersion.

1 INTRODUCTION

The elastic response of porous rocks can be investigated using various experimental methodologies (Born 1941; Winkler & Nur 1979; Harris *et al*. 2005; McCann & Sothcott 2009; Gordon & Davis 2012; Wang *et al*. 2012; Zhao *et al*. 2013; Yin *et al*. 2017, 2019; Sun *et al*. 2018, 2020; Zhao *et al*. 2019; Borgomano *et al*. 2020). One classical method is the forced oscillation technique, which measures the quasi-static axial and radial strains in response to an axially oscillating stress to determine the Young's modulus and Poisson's ratio of rocks in the seismic frequency range (<100 Hz; Spencer 1981; Batzle *et al*. 2006; Mikhaltsevitch *et al*. 2011; Tisato & Madonna 2012; Pimienta *et al*. 2015; Spencer & Shine 2016; Sun *et al*. 2018, 2020, 2022; Zhao *et al*. 2019, 2021; Borgomano *et al*. 2020; Li *et al*. 2020).

Two kinds of sensors in the forced-oscillation method are used to measure strain (Subramaniyan *et al*. 2014): the linear variable differentiator transformer (LVDT) and the strain gauge. The LVDT measures the bulk axial strain, the average axial strain along the entire sample. However, it cannot measure the radial strain necessary for calculating the Poisson's ratio. In contrast, the strain gauge (4–6 mm) can measure both axial and radial strains, making it possible to obtain the Poisson's ratio as demonstrated by various researchers (Batzle *et al*. 2006; Mikhaltsevitch *et al*. 2014; Pimienta *et al*. 2015, 2017; Sun *et al*. 2018; Chapman *et al*. 2019; Borgomano *et al*. 2020). The smaller size of the strain gauge reduces the impact of the 'bending effect' (Kumar 2003) on radial strain measurements. However, the strain gauge may introduce errors in determining attenuation and moduli of samples with heterogeneities larger than the strain gage, such as mesoscopic (a scale that is significantly larger than the

pore scale but much smaller than the wavelength) multiphase fluid distributions or fractures (Pimienta *et al*. 2016; Chapman & Quintal 2018; Sun *et al*. 2020; Gallagher *et al*. 2022; Guo *et al*. 2022a, b).

In this work, we focus on the case of homogeneous and isotropic rock with two-phase immiscible fluids. The fluid distribution in the biphasic saturated rock can be heterogeneous at the mesoscopic scale. It has been validated not only in the previous experiments by Cadoret *et al*. (1998) and Toms-Stewart *et al.* (2009) using computer-assisted tomographic (CT) scanners but also in recent CT experiments conducted by Chapman *et al*. (2021) and Sun *et al*. (2022). The heterogeneous fluid distribution can lead to dispersion and attenuation in response to mesoscopic wave-induced fluid flow (WIFF; e.g. Müller *et al*. 2010). Batzle *et al*. (2006) measured and estimated velocities in sandstone as a function of water saturation by injection. They found that the frequency-dependent velocities support the WIFF theory. Spencer & Shine (2016) measured the effects of partial gas or oil saturation on velocities and attenuation. They observed dispersion and attenuation in partially saturated sandstones attributed to the mesoscopic WIFF. Recently, Chapman *et al*. (2021) conducted experiments on a Berea sandstone sample partially saturated with carbon dioxide following a reduction in pore pressure and attributed the observed attenuation and dispersion to a heterogeneous water distribution. Similarly, Sun *et al*. (2022) investigated a partially saturated limestone through the imbibition and drainage of water. The pronounced dispersion and attenuation were also concluded to be the consequence of the heterogeneous fluid distribution at the mesoscopic scale.

These measurements provide solid experimental evidence for the existence of mesoscopic WIFF. However, most experimental results are obtained from local measurements, that is strain gauges. To investigate the effect of the local strain measurement, Chapman & Quintal (2018) present a 1-D-layer model to investigate the difference between the local and bulk strain measurements for partially saturated samples. They numerically solved Biot (1941)'s quasi-static poroelastic equations and average the stress and strains either over the entire model domain or over discrete slices to determine either the bulk or local response, respectively. They found that the variation of the strain gauge locations could result in a significant difference in the determined dispersion and attenuation related to the mesoscopic WIFF. Chapman *et al*. (2021) later also showed that their experimental observations were in better agreement with numerical simulations where the stress and strain were locally averaged. However, these investigations assumed cylindrical symmetry for the fluid distribution, ignoring saturation variation in the radial direction. In addition, they did not conduct a broad quantitative analysis and assessment of the errors associated with local strain measurements.

To overcome the limitations and further investigate the effect of local measurements, we build a 3-D numerical model based on Biot's poroelastic theory to simulate the forced-oscillation measurement process. It takes the 3-D distribution into account and can estimate the Young's modulus and Poisson's ratio directly, just as in the experiment. Then, we investigate the effect of the strain gauge location, number, and size on the local response for a cylinder sample. The errors in the local and bulk responses of samples saturated with quasi-fractal fluid distributions are quantified. Furthermore, using the Monte Carlo method, we discuss the error between the laboratory scale (local strain measurements) and the reservoir-scale response. Our study aims to provide guidance on the issue of local measurements for rock physicists investigating frequency-dependent effects in biphasic saturated rock using the forced oscillation method.

2 METHODOLOGY

2.1 Numerical model

We developed a numerical model to simulate the mechanical apparatus (Fig. 1a) used in previous studies (Borgomano *et al*. 2020) to measure the elastic properties of porous rocks. The model comprises a shaker, two aluminium end-platens (UOP and DOP in Fig. 1b) and a porous rock specimen (TestS in Fig. 1c). Our model can also be adapted for other low-frequency measurement setups with similar mechanical configurations (e.g. Tisato & Madonna 2012; Mikhaltsevitch *et al*. 2015; Sun *et al*. 2018, 2022; Chapman *et al*. 2021).

2.2 Governing equations

Biot's equations (Biot 1941,1956a, b, 1962) are used to investigate the poroelastic response of the numerical model. The method was widely used to study dispersion and attenuation (e.g. Rubino *et al*. 2009, 2016; Quintal *et al*. 2011; Sun *et al*. 2022). We opt for the displacement-pressure form of Biot's equations (Atalla *et al*. 1998) in the frequency domain to serve as our governing equations. They are given by:

$$-\omega^2\rho_b - \frac{\rho_{\mathrm{f}}^2}{\rho_{\mathrm{c}}(\omega)}\boldsymbol{u}^{\boldsymbol{s}} - \nabla\cdot\sigma = \frac{\rho_{\mathrm{f}}}{\rho_{\mathrm{c}}(\omega)}\nabla P_{\mathrm{f}}, \tag{1}$$

$$\nabla\cdot\left[-\frac{1}{\rho_{\mathrm{c}}(\omega)}\nabla P_{\mathrm{f}} - \omega^2\rho_{\mathrm{f}}\boldsymbol{u}^{\boldsymbol{s}}\right] - \frac{\omega^2\boldsymbol{P}_{\boldsymbol{f}}}{\mathrm{M}} = \alpha\omega^2\nabla\cdot\boldsymbol{u}^{\boldsymbol{s}}, \tag{2}$$

where $\nabla = \frac{\partial}{\partial x}\hat{i} + \frac{\partial}{\partial y}\hat{j} + \frac{\partial}{\partial z}\hat{k}$, where $\hat{i}$, $\hat{j}$ and $\hat{k}$ are the imaginary units at x-, y- and z-directions. ω is the angular frequency, $\alpha = 1 - \frac{K_d}{K_g}$ is the Biot–Willis coefficient, K_d is the drained bulk modulus of the matrix, K_g is the bulk modulus of the grain. The density of the bulk material is $\rho_b = (1-\phi)\rho_{\mathrm{s}} + \phi\rho_{\mathrm{f}}$, where ρ_{f} and ρ_{s} correspond to the densities of the fluid and solid grain, respectively. The complex density $\rho_{\mathrm{c}}(\omega) = \frac{\tau\rho_{\mathrm{f}}}{\phi} + \frac{\eta}{i\omega\kappa}$, where ϕ is the porosity, τ is the tortuosity of the pore, η is the fluid viscosity and κ is the permeability. The stress tensor σ is written in terms of tensor components using index notation as:

$$\sigma_{ij} = 2\mu\varepsilon_{ij} + \delta_{ij}\left(\lambda_m\nabla\cdot\boldsymbol{u}^{\boldsymbol{s}} - \alpha P_{\mathrm{f}}\right), \tag{3}$$

where $i, j = 1, 2, 3$ corresponds to Euclidean space dimensions. The stress tensor is determined by the solid displacement vector $\boldsymbol{u}^{\boldsymbol{s}} = (u_i^s)$, strain tensor $\varepsilon_{ij} = \frac{1}{2}(u^s_{i,j} + u^s_{j,i})$ and fluid pressure P_{f}, $u^s_{i,j}$ is the derivative of u_i^s at j direction. $\lambda_m = K_d - \frac{2}{3}\mu$ is the first parameter of Lamé constants, and μ is the shear modulus. δ_{ij} is the Kronecker Delta. The so-called pore-space modulus (Biot & Willis 1957; Gurevich *et al*. 2009) is defined by:

$$\mathrm{M} = \left(\frac{\phi}{K_{\mathrm{f}}} + \frac{\alpha-\phi}{K_g}\right)^{-1}, \tag{4}$$

where the bulk modulus K_{f} and density ρ_{f} of the biphasic fluids are given by:

$$K_{\mathrm{f}} = \left(\frac{S_{\mathrm{Air}}}{K_{\mathrm{Air}}} + \frac{1-S_{\mathrm{Air}}}{K_{\mathrm{w}}}\right)^{-1}, \tag{5}$$

$$\rho_{\mathrm{f}} = \rho_{\mathrm{Air}}S_{\mathrm{Air}} + \rho_{\mathrm{w}}(1-S_{\mathrm{Air}}), \tag{6}$$

where K_{Air} and K_{w} are the bulk modulus of air and water, respectively, S_{Air} is the air saturation. ρ_{Air} and ρ_{w} are the densities of water and air, respectively. The viscosity η of the biphasic fluids is defined according to Teja & Rice (1981):

$$\eta = \eta_{\mathrm{Air}}\left(\frac{\eta_{\mathrm{w}}}{\eta_{\mathrm{Air}}}\right)^{1-S_{\mathrm{Air}}}, \tag{7}$$

where η_{Air} and η_{w} are the viscosities of air and water, respectively.

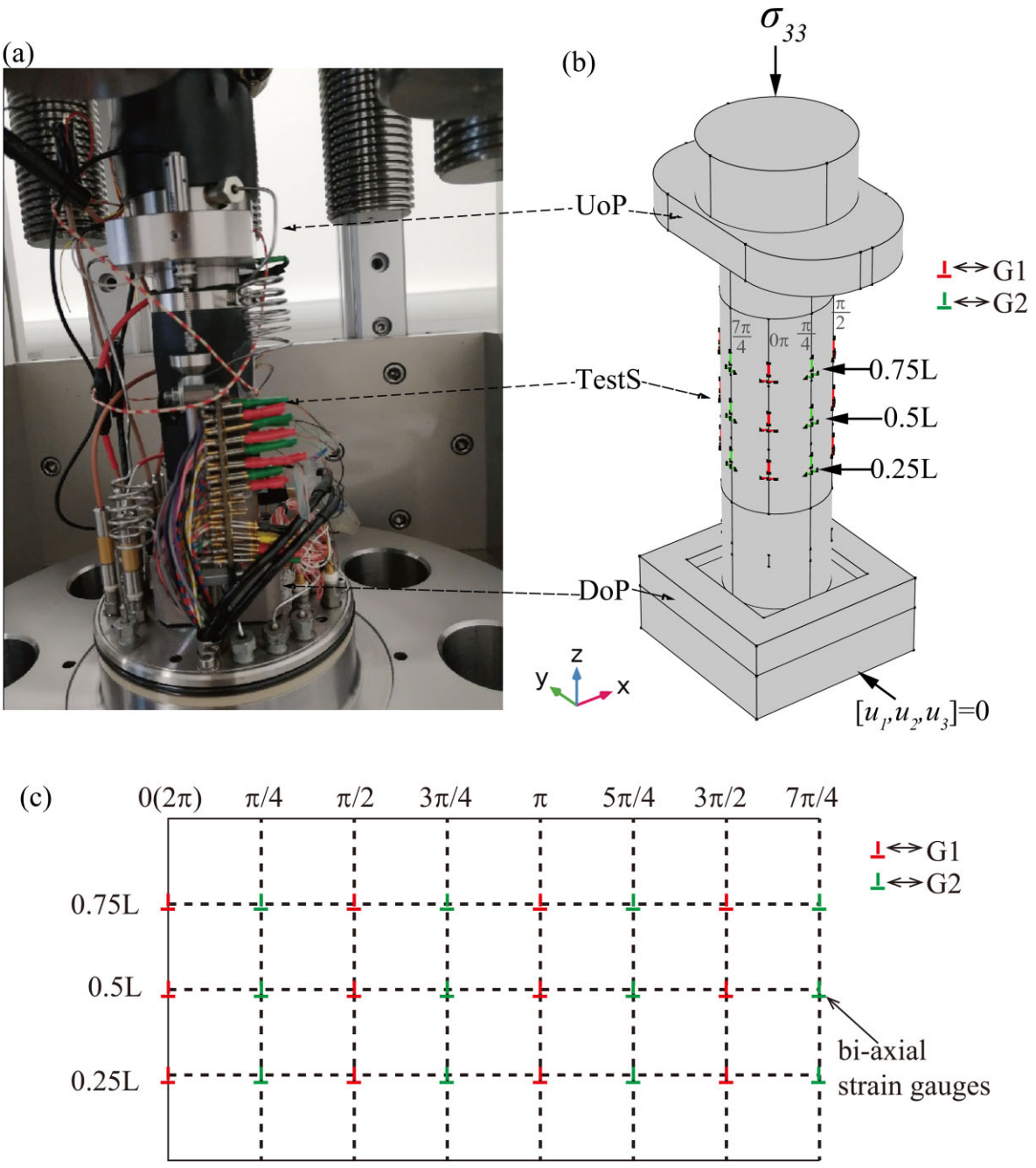

Figure 1. (a) Low-frequency measurement cell. The piezoelectric actuator generates the axial oscillation, and the strain gauges record the corresponding axial and radial strains; (b) the 3-D numerical model of (a). The UOP and DOP are the up and down end-platens, respectively. TestS is the cylinder specimen. σ_{33} is the axial oscillation stress loading at the top surface of up end-platens (UOP). [u1, u2, u3] = 0 is the fixed boundary condition for bottom end-platends (DOP). The 0.25 L, 0.5 L and 0.75 L are the vertical positions at 25, 50 and 75 per cent of the sample length. G1 are strain gauges placed at 0, $\frac{\pi}{2}$, π and $\frac{3\pi}{2}$, while G2 are strain gauges placed at $\frac{\pi}{4}$, $\frac{3\pi}{4}$, $\frac{5\pi}{4}$ and $\frac{7\pi}{4}$. (c) 2-D view of the cylindrical test sample.

2.3 Numerical model configuration and solution

We used COMSOL Multiphysics to solve the governing equations (eqs 1 and 2) with the finite element method and simulate an axial oscillatory test, allowing us to compute the Young's modulus and Poisson's ratio as a function of frequency.

To impose the necessary boundary conditions, we applied the following configuration: On the top surface of the UoP (Fig. 1b), we applied an axially oscillating stress with an amplitude of 0.1 MPa; At the bottom surface of the DoP (Fig. 1b), the displacement vector $\boldsymbol{u}^s$ is zero. To simulate undrained boundary conditions, we assign the fluid pressure gradient $\nabla P_f = 0$ on all the surfaces of the test sample (TestS in Fig. b); For the Aluminium end-platens (UOP and DOP in Fig. 1b) in the numerical model, the fluid pressure P_f is zero (Quintal *et al.*, 2011), causing eq. (1) to degenerate into the elastic equation. Under these boundary conditions, eq. (1) maintains stress continuity at the interface between the test sample and Aluminium end-platens.

The strains determined from the numerical solutions are used to calculate the frequency-dependent Young's modulus $E(\omega)$ and the

Table 1 Properties for the aluminium and test sample.

Properties	Aluminium (stress standard)	Test sample
Porosity, ϕ (per cent)	0	10.8
Permeability, κ (m^2)	0	2.27×10^{-16}
Drained bulk modulus, K_d (GPa)	70.6	24
Undrained bulk modulus, K_u (GPa)	70.6	32.5
Bulk modulus of grain, K_g (GPa)	70.6	77
Shear modulus, G (GPa)	27.1	15.2
Drained Young's modulus, E (GPa)	72	37.5
Drained Poisson's ratio, ν	0.33	0.24
Biot–Willis coefficient, α	0	0.69
Skempton's coefficient, B	0	0.38
Density, ρ (kg m^{-3})	2700	2369.2

corresponding attenuation $Q_{\mathrm{E}}^{-1}(\omega)$, the Poisson's ratio $\nu(\omega)$ and the corresponding phase difference Q_{ν}^{-1} by:

$$E(\omega) = \frac{E_{al}}{\langle \varepsilon_{33} \rangle_{\mathrm{Alum}}} \langle \varepsilon_{33} \rangle_{\mathrm{Sam}} \tag{8}$$

$$Q_{\mathrm{E}}^{-1}(\omega) = \frac{\mathrm{Imag}\,(E(\omega))}{\mathrm{Real}\,(\mathrm{E}(\omega))} \tag{9}$$

$$\nu(\omega) = \frac{\langle \varepsilon_{11} \rangle_{\mathrm{Sam}}}{\langle \varepsilon_{33} \rangle_{\mathrm{Sam}}} \tag{10}$$

$$Q_{\nu}^{-1}(\omega) = \frac{\mathrm{Imag}\,(\nu(\omega))}{\mathrm{Real}\,(\nu(\omega))}, \tag{11}$$

where $E_{al} = 72$ GPa is the Young's modulus of the aluminium end-platen, $\langle\,\rangle$ is the average operator. $\langle \varepsilon_{33} \rangle_{\mathrm{sam}}$ and $\langle \varepsilon_{33} \rangle_{\mathrm{Alum}}$ are the axial strains of the test sample and the aluminium end-platen, respectively. $\langle \varepsilon_{11} \rangle_{\mathrm{Sam}}$ is the radial strain of the test sample. The strains are averaged over the entire model domain to determine the bulk response. The strains are averaged over small sections of the sample's domain to determine the local response measured by strain gauges in a laboratory experiment (Fig. 1b). We used a tetrahedral mesh refined according to the fluid distribution, with a higher mesh resolution at water–air interfaces. Mesh resolution is also enhanced over regions corresponding to the strain gauges.

2.4 Validating the numerical solution

To validate our numerical procedure, we compare our numerical solution to the analytical solution of Dutta & Odé (1979). The validation is performed on a homogenous and isotropic cylinder with a 20 mm radius and 80 mm length. The properties of the rock matrix are shown in Table 1. We assumed that the cylinder sample contains two spheres with a radius of 11 mm (Fig. 2a). The spheres are saturated with air (blue domains, Fig. 2a), whereas the remaining regions are saturated with water. The fluid properties are shown in Table 2. The air saturation can be estimated using the ratio of the sphere's volume to the cylinder's volume, that is, $\mathrm{S_{Air}} = 2 \times \frac{\frac{4}{3}\pi(0.011)^3}{\pi \times 0.02^2 \times 0.08} = 0.11$. According to the assumption in Dutta & Odé (1979)'s model, the representative elementary volume (REV) of the cylinder is shown in Fig. 2(b), and the patchy size can be approximated by $\sqrt[3]{\frac{\frac{4}{3}\pi(0.011)^3}{\mathrm{S_{Air}}}} = 37$ mm.

Next, we calculated the Young's modulus E and the Poisson's ratio υ in the case of a sample as described in Fig. 2(a) at the frequencies of 0.01–1000 Hz. The *P*-wave modulus is deduced by $\frac{E(1-\upsilon)}{(1+\upsilon)(1-2\upsilon)}$ (Mavko *et al*. 2009). Then, we compared the numerical results with the analytical solution obtained from Dutta & Odé's (1979) model. Fig. 3(a) displays the dispersion of the *P*-wave modulus, and Fig. 3(b) shows the associated attenuation. The squares are the numerical results, and the solid lines are the analytical solutions. We can observe an excellent matching between the analytical and numerical solutions, and the peak in *P*-wave attenuation agrees with the theoretical prediction (Dutta & Odé 1979).

To validate the accuracy of our numerical model's ability to reproduce physical measurements, we used data published by Sun *et al*. (2022) for comparison. The bulk modulus and attenuation of the limestone, which were measured using four strain gauges, are represented by squares in Figs 3(c) and (d), respectively. The properties of the limestone (test sample) are shown in Table 1. We used these properties to generate predictions with our numerical model, the results of which are represented as red lines in Figs 3(c) and (d). The predicted bulk modulus and corresponding attenuation are in alignment with the measurements, further validating the reliability of our numerical model. Notably, these predictions heavily rely on the fluid distribution depicted in the CT images provided by Sun *et al*. (2022). Ideally, CT images are the optimal tool for evaluating the impact of fluid heterogeneity. However, their extensive usage is impractical due to high costs, necessitating an alternate approach. According to prior research (e.g. Müller *et al*. 2008; Toms *et al*. 2009), the spatial correlation of fluid distribution can be characterized by either the von Kármán function or the Debye function. In the drainage CT case presented by Sun *et al*. (2022), the spatial correlation estimated using Toms *et al*.'s (2009) method can be fitted with the von Kármán function, yielding a correlation length of 1.4 mm and a Hurst number of 0.8. Consequently, we adopt the von Kármán function to delve into the effects of fluid heterogeneity in subsequent sections.

2.5 The quasi-fractal fluid distribution

We assume that the biphasic fluid distribution is a self-affine monofractal and can be characterized using the von Kármán function. According to previous research (e.g. Klimeš 2002; Helle *et al*. 2003; Santos *et al*. 2005; Müller *et al*. 2008; Rubino *et al*. 2009), the steps for generating the 3-D heterogeneous fluid distribution can be summarized as follows:

(i) A spatial field, $W(x, y, z)$, is populated with random numbers derived from a uniform distribution, also known as white noise. Here, x, y and z are coordinates in the Cartesian coordinate system.

(ii) This spatial field W is then subjected to a Fourier transformation, mapping it to the spatial wavenumber domain, represented as $\hat{W}(k_x, k_y, k_z)$. In this context, k_x, k_y and k_z denote the wavenumbers in the x-, y- and z-directions, respectively.

(iii) Subsequently, we apply the von Karman spectrum filter, $S = S_0(1 + k^2 l_{\mathrm{c}}^2)^{-(H+3/2)}$, to $\hat{W}$. Here, S_0 is a normalization constant, $k = \sqrt{k_x^2 + k_y^2 + k_z^2}$ is the amplitude of the wavenumber, l_{c} is the correlation length (a measure of the length scale of heterogeneity as per Müller *et al*. 2008), and H is the Hurst exponent ($0 < H < 1$). The fractal dimension of the stochastic field for the 3-D case can be given by $D = 4 - H$ (Rubino *et al*. 2009). As a result, we obtain

$$\hat{U}(k_x, k_y, k_z) = \hat{W} S. \tag{12}$$

(iv) Finally, the filtered result $\hat{U}$ is then transformed back to the spatial domain $U(x, y, z)$, forced to have zero means, and normalized to a range appropriate to produce a saturation with fluctuations around a given global air saturation S^*. To construct the patches, we set the air saturation to one for regions where $S < S^*$, and zero for regions where $S > S^*$ (Santos *et al*. 2005). Following this, we

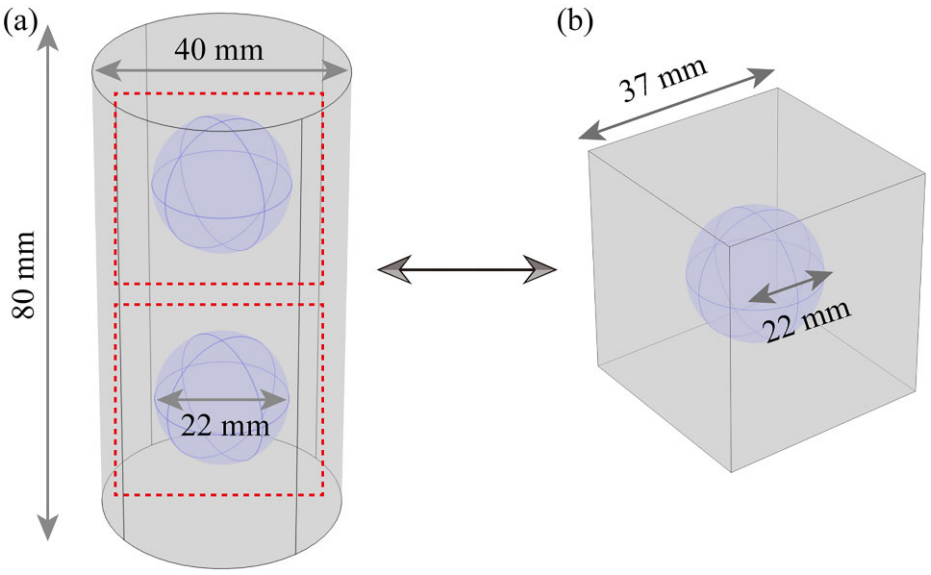

Figure 2. (a) The homogenous and isotropic rock containing two air spheres. The cylinder is 40 mm in diameter and 80 mm in length. The sphere is 22 mm in diameter; (b) the REV size of 37 mm.

Table 2 Properties for the fluid.

Properties	Water	Air
Bulk modulus, K_f (GPa)	2.25	1×10^{-4}
Density, ρ (kg m^{-3})	1000	1
Viscosity, η (Pa s)	10^{-3}	2×10^{-5}

shape the cube to form the cylinder sample, which facilitates simulation consistency with the experiment and helps avoid the 'oversized problem' (Ravalec *et al*. 2000) at the start and end of the domain.

3 RESULTS AND ANALYSIS

In the numerical test, the diameter and length of the test sample are 4 and 8 cm, respectively. The other properties, such as permeability and porosity, are given in Table 1. We set $H = 0.8$, $l_c = 10$ mm, $S^* = 0.11$ and $D = 3.2$ to generate the fluid distribution following the method described in Section 2.5. The resulting fluid distribution is shown in Fig. 4(a). The global water saturation is $S_w = 1 - S^* = 0.89$. The black regions and white regions of Fig. 4(a) represent zones fully saturated by water and air, respectively. The adaptive mesh corresponds to the fluid distribution (Fig. 4a) shown in Fig. 4(b), where the mesh is refined at the water–air interfaces. Next, we illustrate how accurately we can approximate the bulk response using a strain gauge, using the fluid distribution given in Fig. 4(a).

3.1 Strain and fluid pressure

Taking the fluid distribution (Fig. 4a) as an input, we solved the numerical model and obtained the fluid pressure and the axial and radial strains. We normalized the fluid pressure by $\frac{P_f}{\sigma_{33}}$, where the P_f is the fluid pressure, σ_{33} is the axial stress. The diameter of the up-end-platen (UoP in Fig. 1b) is 56 mm, and there is an oscillating axial stress of 0.1 MPa amplitude on its top surface. Then the axial stress σ_{33} amplitude on the sample is given by $\frac{0.028^2}{0.02^2} \times 0.1[\text{MPa}] = 0.196$ MPa. Fig. 5 shows the normalized fluid pressure. For a frequency of 1 Hz (Fig. 5a), the fluid pressure is zero, distributing over the entire sample homogeneously. For a frequency of 1000 Hz, as shown in Fig. 5(d), the fluid pressure is heterogeneously distributed: the normalized fluid pressure is zero in the air-saturated zones and 0.127 in almost all the water-saturated zones. For the water-saturated regions, we can readily calculate Skempton's coefficient according to the definition of normalized fluid pressure (Skempton 1954; Wang 2000) as $B = \frac{3P_f}{\sigma_{33}} = 3 \times 0.127 = 0.38$. This value aligns with the poroelastic properties of the rock, $\text{B} = \frac{1-\frac{K_d}{K_u}}{\alpha} = 0.38$ (Table 1), suggesting that water-saturated zones are in an undrained state at a frequency of 1000 Hz. The heterogeneity of the fluid pressure distribution, as shown in Figs 5(b) and (c), is frequency-dependent, and this heterogeneity increases with frequency.

The axial strain ε_{33} (Fig. 6) as well as radial strain ε_{11} (Fig. 7) vary spatially, exhibiting the heterogeneity associated with the fluid distribution (Fig. 5). At the frequency of 1 Hz, the axial strain (Fig. 6a) and radial strain (Fig. 7a) distribute homogeneously over the sample at 52×10^{-7} and 12.5×10^{-7}, respectively, and agree with the drained sample's properties (Table 1). At 1000 Hz, the axial and radial strains (Figs 6d and 7d) distribute over the sample heterogeneously. In the water-saturated zones, the axial and radial strains are $\sim 50 \times 10^{-7}$ and $\sim 14.7 \times 10^{-7}$, respectively, and agree with the undrained sample's properties (Table 1). As for the fluid pressure, the heterogeneity in the sample's strain distribution increases with frequency.

The heterogeneity in strains and fluid pressure will lead to inaccuracies due to the strain gauges' limited coverage of the sample's surface. For comparison, we can obtain the bulk response (red lines, Fig. 8) by averaging the strain over the entire sample. With the increase in frequency from 0.01 to 1000 Hz, Young's modulus increases from 37.5 to 39 GPa, and the Poisson's ratio increases from 0.24 to 0.286 (red curves in Fig. 8). The Young's attenuation peak is 0.014 at the critical frequency of 10 Hz. The Poisson's ratio phase difference shows an attenuation peak of 0.06 at the same critical frequency of 10 Hz.

3.2 The effect of the strain gauge locations

Bi-axial strain gauges with a typical length of 5 mm measure both the vertical and horizontal strain. They were simulated using 5 mm lines on the lateral surface of the cylindrical sample, as depicted

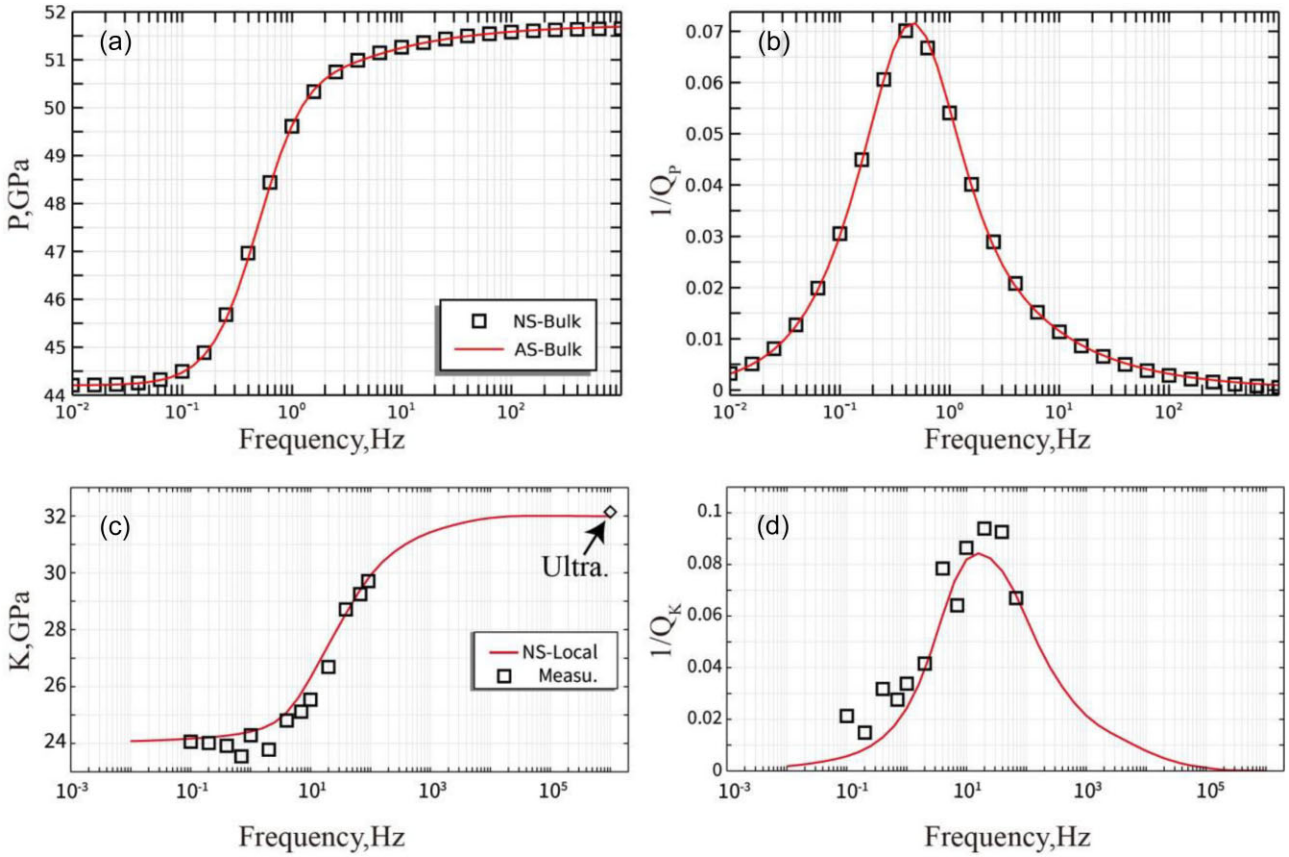

Figure 3. *P*-wave modulus (a) and *P*-wave attenuation (b) at the frequencies of 0.01–1000 Hz. They are obtained from the numerical model (squares) and Dutta & Odé's (1979) model (red line). Bulk modulus (c) and bulk attenuation (d) are adapted from fig. 18 in the research of Sun *et al*. (2022). The black squares represent measurements taken when the Indiana sample is partially saturated with a water saturation level of 88 per cent. The red lines illustrate predictions made using the fluid distribution, ascertained from CT scans displayed in fig. 12 of Sun *et al*.'s (2022).

in Fig. 1(c): strain values were averaged over these 5 mm lines to simulate the recording of bi-axial strain gauges. Using eqs (8)–(11), we calculated the values of Young's modulus, Young's attenuation, Poisson's ratio, and Poisson's phase difference recorded by the strain gauges. To study the effect of strain gauge location, we specifically examined the strain gauges belonging to G1 in Fig. 1(c).

At the location of 0.25 L in Fig. 1(c) (G1 strain gages are the red crosses), we determined the Young's modulus and Poisson's ratio by averaging the four axial and radial strain gauges values. The resulting Young's modulus (indicated by asterisks in Fig. 8a) were almost identical to the bulk response values (shown as a red line in Fig. 8a). The attenuation values (depicted as asterisks in Fig. 8b) also exhibited a peak of 0.014 at 10 Hz, which agreed with the bulk response values (represented by a red line in Fig. 8b). However, the Poisson's ratio values (illustrated as asterisks in Fig. 8c) displayed two dispersion transitions. Correspondingly, the Poisson's phase difference (asterisks, Fig. 8d) displays two peaks with the magnitudes of 0.07 and 0.025 at 7 and 200 Hz, deviating significantly from the peak of 0.062 at 10 Hz for the bulk response (red line, Fig. 8d). At 0.5 L, the Young's modulus (circles, Fig. 8a) is more dispersive in comparison to the bulk response (red line, Fig. 8a). The corresponding Young's attenuation (circles, Fig. 8b) is overestimated compared to the bulk attenuation (red line, Fig. 8b). The Poisson's ratio and the Poisson's phase difference are also overestimated with respect to the bulk response. At 0.75 L, the Young's modulus (solid squares, Fig. 8a) is less dispersive than the bulk response, and the corresponding attenuation (solid squares, Fig. 8b) is underestimated with respect to the bulk response. However, the Poisson's ratio (solid squares, Fig. 8c) is more dispersive than the bulk response, and the Poisson's phase difference (solid squares, Fig. 8d) shows a higher peak at the critical frequency of 10 Hz. The local responses at 0.25, 0.5 and 0.75 L differ significantly from each other and the bulk response, showing that the local response significantly depends on the vertical location of the sample. The conclusion is consistent with the result given by Chapman & Quintal (2018) using a 1-D model.

In summary, the Young's modulus, Young's attenuation, Poisson's ratio and Poisson's phase difference depending on the locations of the strain gauges, making it challenging to obtain the bulk response from the local measurements. The question is: Can we quantify the error made when strain gauges are used to infer the bulk response? And: How does strain gauge number and length affect this error?

3.3 The effect of the strain gauge number

How many strain gauges are required to obtain an accurate bulk response? We randomly selected 1, 4, 8, 12, 16 and 20 bi-axial strain gauges in groups G1 or G2 from Fig. 1(c) and calculated averaged values for the Young's modulus, Young's attenuation, Poisson's ratio and Poisson's phase difference. The results are shown in Fig. 9.

When only one strain gauge is used, the dispersion for Young's modulus and corresponding Young's attenuation is overestimated compared to the bulk response. As the number of strain gauges

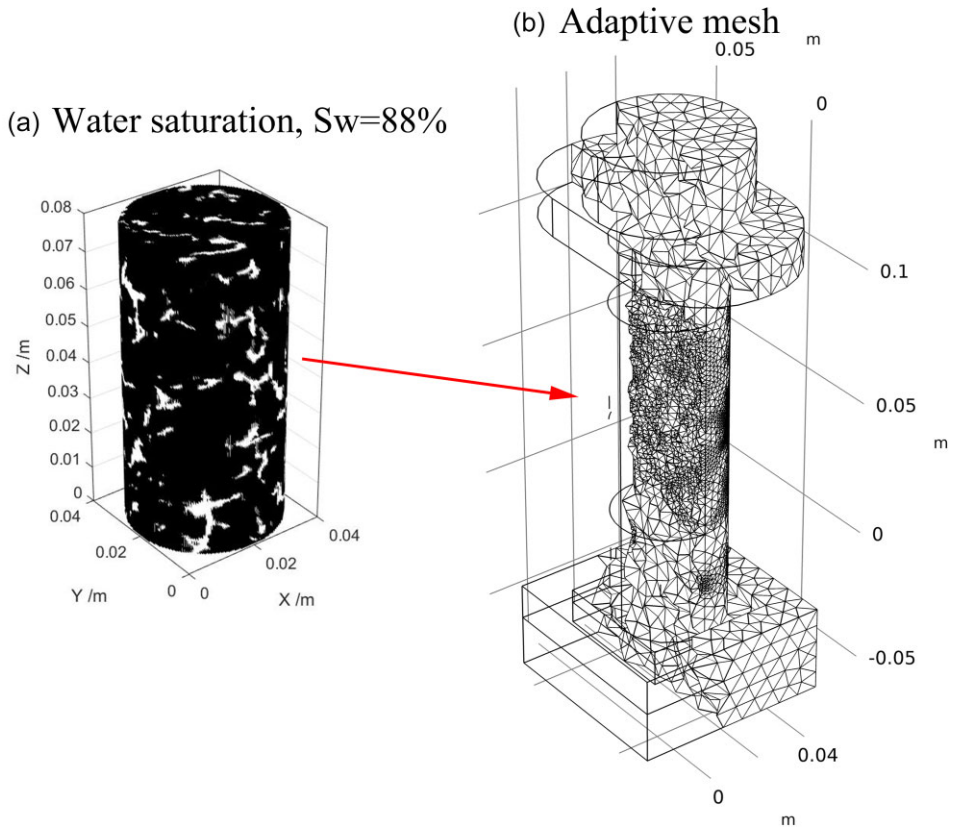

Figure 4. (a) Fluid distribution generated by the von Kármán spectrum density function. The Hurst exponent H is 0.8, the correlation length l_c is 10 mm, the water saturation is 0.89, and the fractal dimension D is 3.2. Black zones represent water, while white zones represent air. (b) The adaptive mesh, with the water–air interfaces refined according to the fluid distribution in (a).

increased from 1 to 4, the local responses of both the Young's modulus and the Poisson's ratio and their attenuations approached the bulk response (Fig. 9a), especially for frequencies below 100 Hz. As the number of strain gauges increased from 4 to 21, the local responses of both the Young's modulus and the Poisson's ratio are close to the bulk response even for frequencies higher than 100 Hz. As expected, increasing the number of strain gauges reduces the difference between local and bulk responses.

To quantify the effect of the strain gauge number, we defined the absolute error between the local measurement and the bulk response over all frequencies as:

$$\varepsilon_\beta = \sqrt{\frac{1}{N_\mathrm{F}} \sum_{m=1}^{N_\mathrm{F}} [\beta^B(f_m) - \beta^L(f_m)]^2}, \tag{13}$$

where N_F is the total number of frequencies investigated. $\beta^L(f_m)$ and $\beta^B(f_m)$ correspond to the local and bulk response at a particular frequency of f_m ($m = 1, \ldots, N_\mathrm{F}$), respectively.

Since the dispersion for the modulus can be as low as a few GPa, while the actual value of the modulus is usually in the tens of GPa range, the absolute error is often relatively small, and it may not provide a comprehensive understanding of the influence of local measurements. To address this, we introduce the relative error over all frequencies, emphasizing the proportion of absolute error in the dispersion or attenuation. Specifically, we define the relative error as:

$$\delta_\beta = \frac{\varepsilon_\beta}{\sqrt{\frac{1}{N_\mathrm{F}} \sum_{m=1}^{N_\mathrm{F}} [\beta^B(f_m) - \mathrm{LLM}]^2}} \times 100\,\text{per cent}, \tag{14}$$

where the LLM is the low-frequency limit for the bulk response $\beta^B(f_m)$. For example, when $\beta^B(f_m)$ is the Young's modulus at f_m, the LLM is the drained Young's modulus. When $\beta^B(f_m)$ is the Young's attenuation, and the LLM is zero attenuation. For the N_s strain gauges, we define the local response by

$$\beta^L(f_m) = \frac{1}{N_s} \sum_{n=1}^{N_s} \beta^n(f_m), \tag{15}$$

where N_s is the total number of the strain gauges, $n = 1, \ldots, N_s$. For each strain gauge n, $\beta^n(f_m)$ is the elastic response at a specific frequency f_m ($m = 1, \ldots, N_\mathrm{F}$), then $\beta^L(f_m)$ is the local response averaged by N_s strain gauges.

We randomly selected a varying number of strain gauges from the 24 available in Fig. 1(c) and calculated the relative error over all frequencies. This process was repeated three times; the results are displayed in Fig. 10. Overall, we observed that the relative error of Young's modulus decreased rapidly from 60 per cent to approximately 10 per cent as the number of strain gauges increased from 1 to 6. However, the error remained at 10 per cent as the number of strain gauges increased from 6 to 24. Therefore, we determined that the critical number of strain gauges required for the accurate measurements of the Young's modulus in the case of Fig. 1 is approximately 6.

Similarly, the critical number of strain gauges for the Poisson's ratio is around 6, above which the relative error decreased from 80 to 20 per cent. Thus, we recommend randomly pasting approximately at least 6 strain gauges and averaging their readings during actual experiments to obtain local responses with minimal error compared

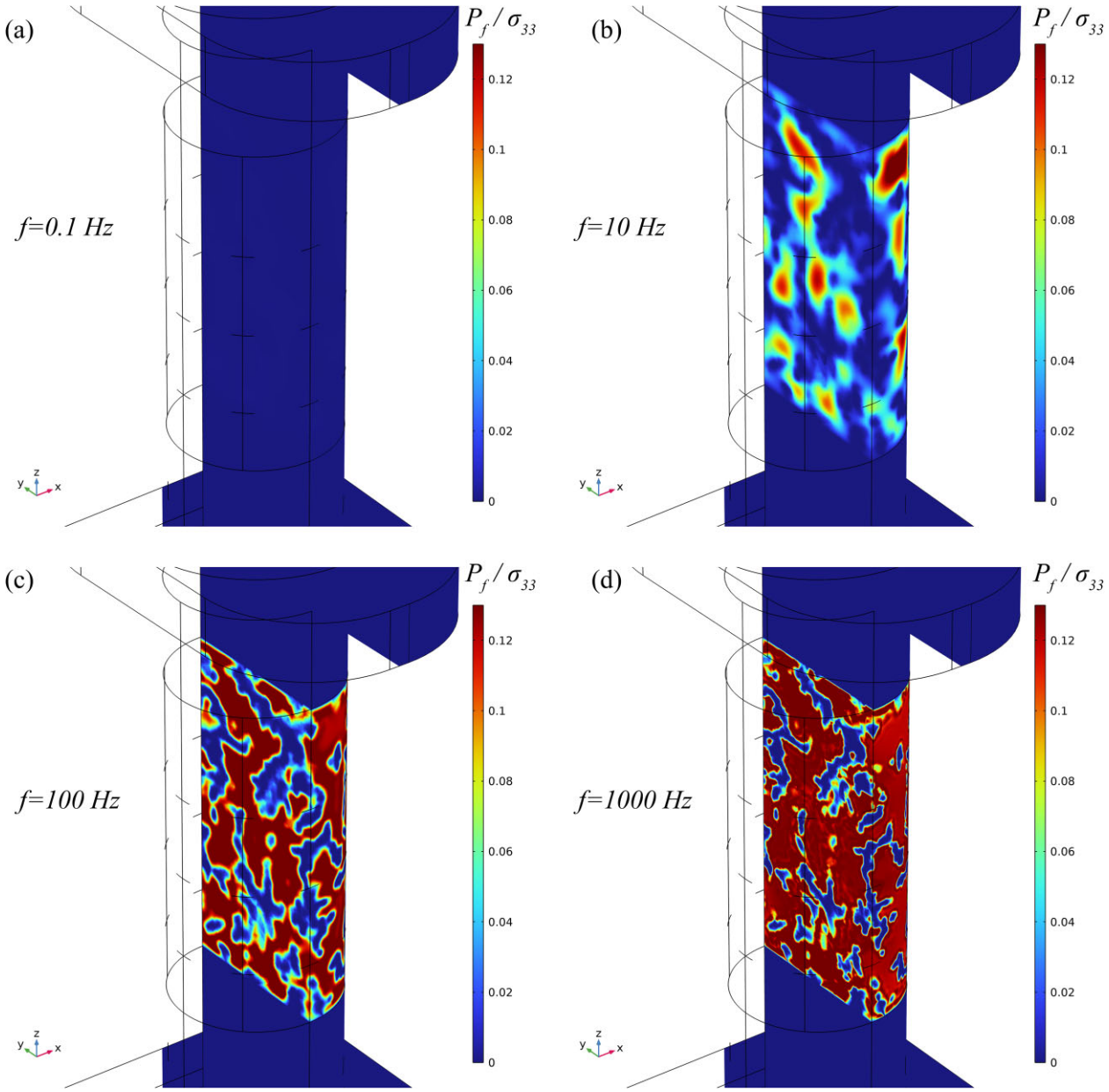

Figure 5. The spatial distribution of the fluid pressure $\boldsymbol{P}_f$ normalized with with respect to the axial stress σ_{33}, at different frequencies: (a) 0.1 Hz; (b) 10 Hz; (c) 100 Hz and (d) 1000 Hz.

to the bulk response. However, it is important to note that this recommendation is specific to the quasi-fractal fluid distribution with a correlation length of 1 cm and strain length of 5 mm used in our study. Variations in the strain gauge length and correlation length could impact the optimal strain gauge number.

3.4 The effect of the strain gauge sizes

Apart from the number of strain gauges, the size of the strain gauge is another important factor that can affect strain measurement accuracy. While it is relatively straightforward to replace a vertically oriented short strain gauge (typically 5 mm in length) with a longer one (e.g. 26 mm in length), the use of a long strain gauge horizontally to measure radial strain is not recommended due to the 'bending effect' (Kumar 2003). As such, we focused our analysis on the effect of varying only the length of the axial strain gauge.

To explore the influence of strain gauge length on our measurements, we focused on the gauge located at the centre of the sample (0.5 L in Fig. 1c). The sample surface was equipped with eight bi-axial strain gauges, a number that is near the critical value previously established in Section 3.3. By averaging the strains recorded by these gauges, we derived the Young's modulus, Young's attenuation, Poisson's ratio and Poisson's phase difference. The results are shown in Fig. 11: the difference between the local and bulk responses for the Young's modulus and attenuation gradually reduced as the axial strain gauge length increased from 5 to 80 mm.

To quantitatively demonstrate the effect of the strain gauge length, we calculated the evolution of relative errors versus the axial strain length according to eq. (14), where $\beta^L(f_m)$ is the local response with different lengths of strain gauges. The result is shown in Fig. 12.

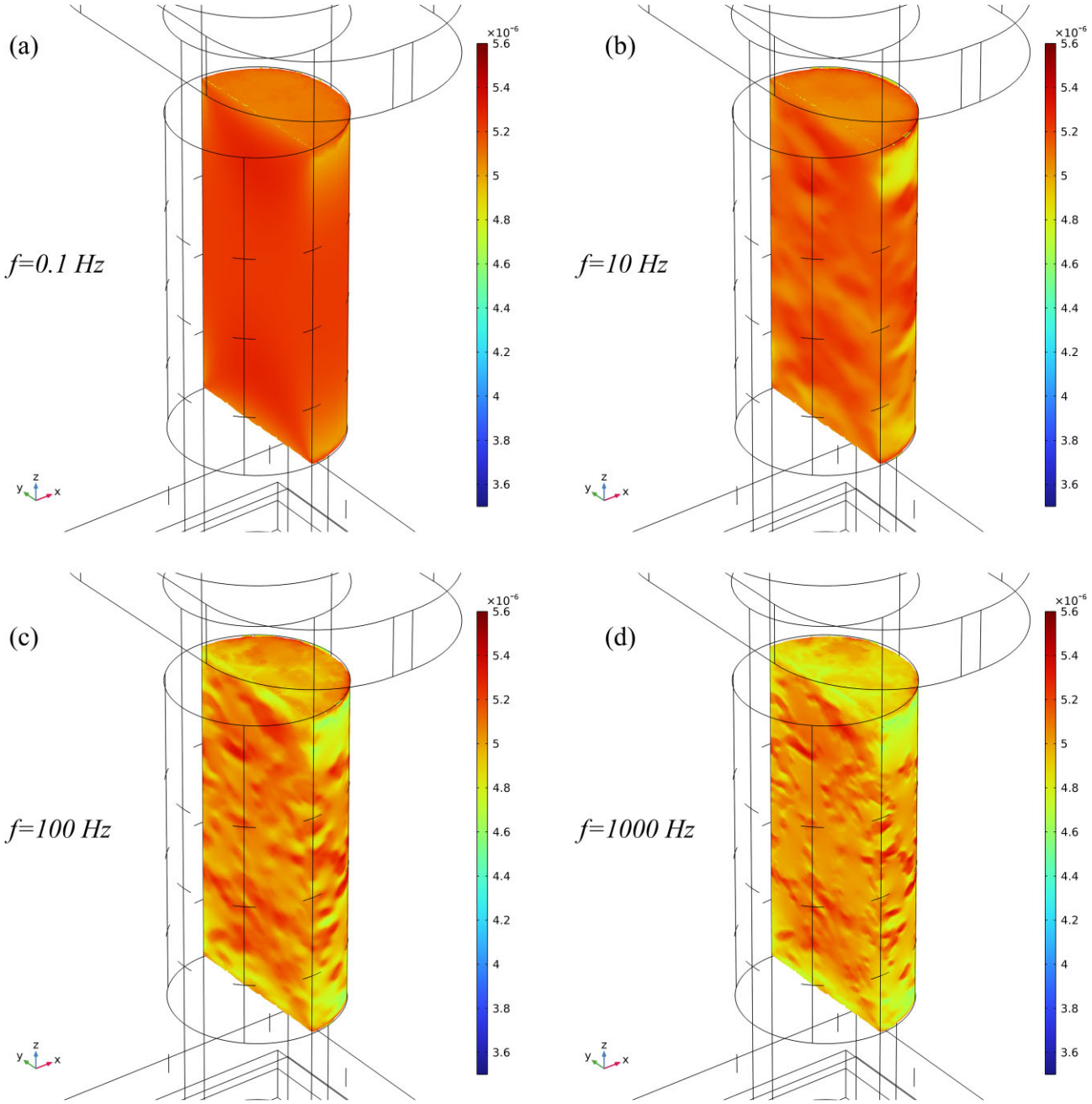

Figure 6. Spatial distribution of the axial strain at different frequencies: (a) 0.1 Hz; (b) 10 Hz; (c) 100 Hz and (d) 1000 Hz.

We found that increasing the axial gauge length from 5 to 26 mm led to a rapid reduction in the relative error of the Young's modulus (Fig. 12a), from 24 to 7 per cent. However, further increasing the axial gauge length to 80 mm did not significantly reduce the relative error of the Young's modulus. The axial gauge length did not significantly affect the relative error in the Poisson's ratio. It indicates that the length of the axial strain gauge has a minimal influence on the local response of the Poisson's ratio as the radial strain gauges length is kept constant at 5 mm in these simulations. To summarize, our results indicate that extending the length of strain gauges from 5 mm to 26 mm can decrease the relative error from ∼20 per cent (with approximately 6–10 strain gauges of 5 mm length) to ∼7 per cent.

4 DISCUSSION

The error between local and bulk responses is influenced by fluid heterogeneity. To obtain the bulk response of a natural reservoir in the lab, the cored rock sample must be at least the size of the reservoir's representative elementary volume (REV), as defined by Hill (1963). In our research context, we disregard rock matrix heterogeneities such as fractures. The REV represents the minimum volume for which (i) fluid heterogeneity is representative of the entire reservoir and (ii) estimated seismic dispersion and attenuation are independent of boundary conditions. However, local strain gauge measurements may still introduce errors even if the sample's volume exceeds the REV size. This section discusses the error between laboratory-scale and reservoir-scale responses under three

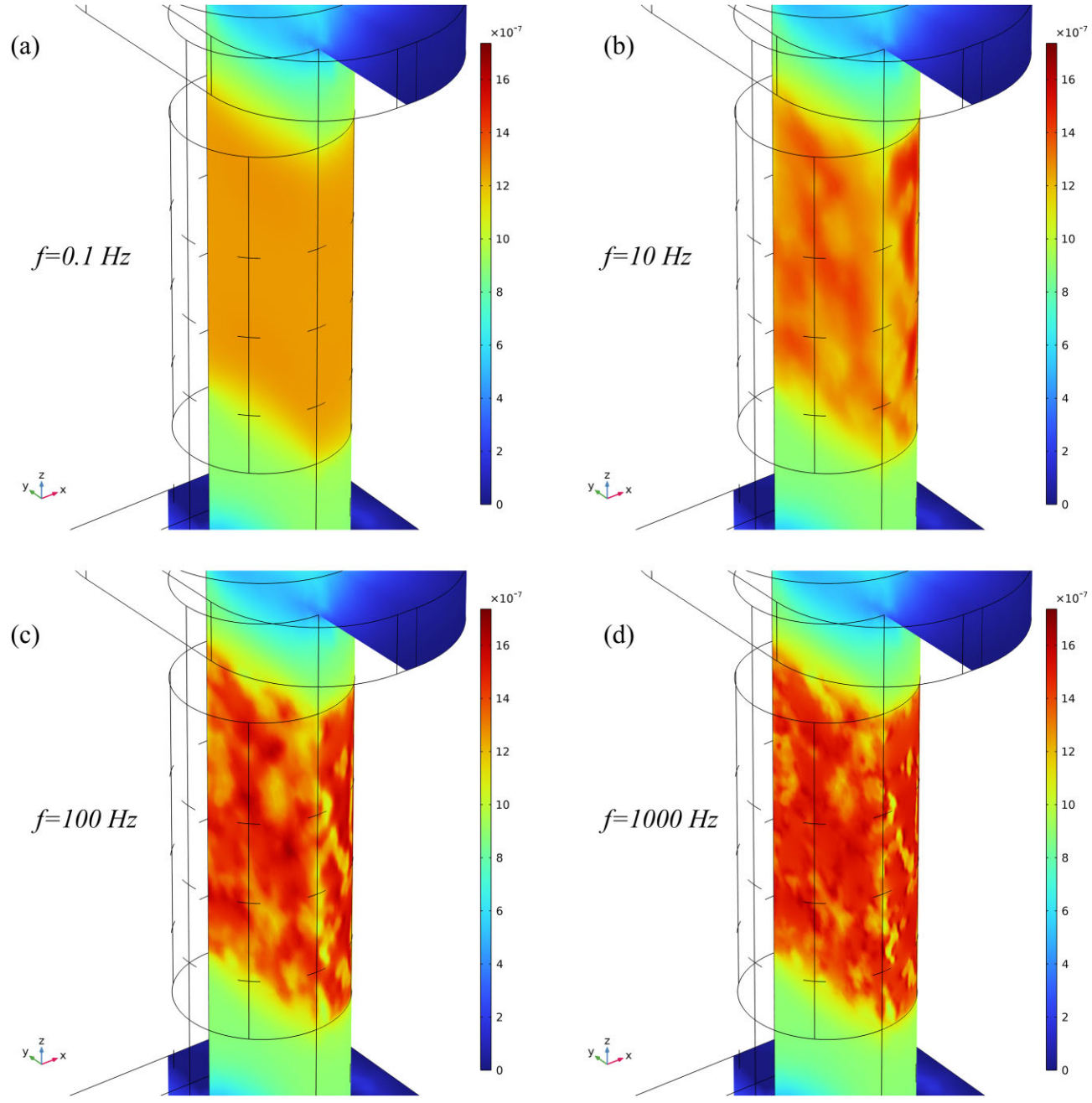

Figure 7. Spatial distribution of the radial strain at different frequencies: (a) 0.1 Hz; (b) 10 Hz; (c) 100 Hz and (d) 1000 Hz.

scenarios: (a) one strain gauge; (b) four strain gauges and (c) four longer strain gauges.

4.1 The effect of the sample number

Previous researchers (e.g. Helle *et al*. 2003; Masson & Pride 2007) suggest that the spatial fluid distribution in a reservoir can be characterized by the stochastic functions (parameter) with a given spectral density distribution, such as the von Karman correlation function used in our study. Accordingly, the Monte Carlo method can predict the equivalent elastic moduli of the partially saturated reservoir (Rubino *et al*. 2009). In this study, we used a two-step approach to demonstrate the application of the Monte Carlo method in investigating the relative error between local measurements and bulk responses at the reservoir scale.

First, we build a cuboid of 0.4 m in length and width and 0.32 m in height. In the cuboid, the von Karman correlation function generates the fluid distribution with $D = 3.2$, $H = 0.8$, and air saturation of 0.12. For the correlation length of 10 and 30 mm, the generated fluid distributions are illustrated in Fig. 13. The black regions represent the water-saturated zones, and the white regions for the air-saturated zones. The fluid distribution becomes more heterogeneous with the increase in the correlation length from 10 mm (Fig. 13a) to 30 mm (Fig. 13c). The cuboid (Figs 13a or c) can provide 400 cylindrical samples with a diameter of 0.04 m and a length of 0.08 m. We randomly selected 70 samples with air saturation of around 12 per cent, as shown in Figs 13(b) and (d), which have similar

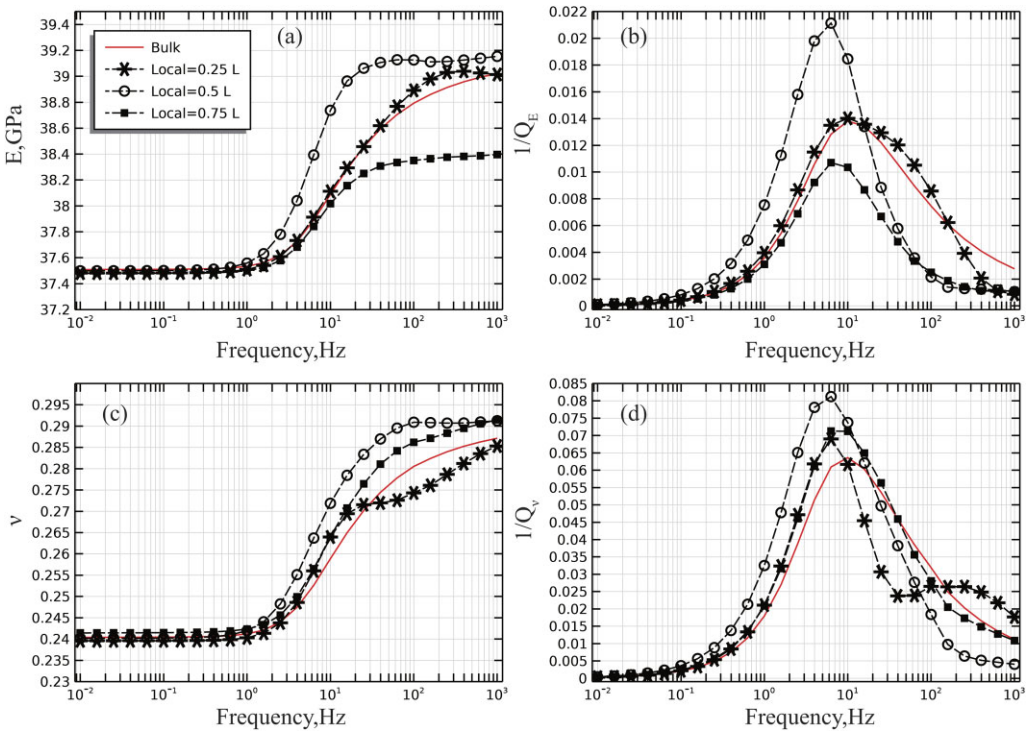

Figure 8. The calculated (a) Young's modulus, (b) Young's attenuation, (c) Poisson's ratio and (d) Poisson's phase difference at 25, 50 and 75 per cent of the sample length. The red line is the bulk response over the entire sample.

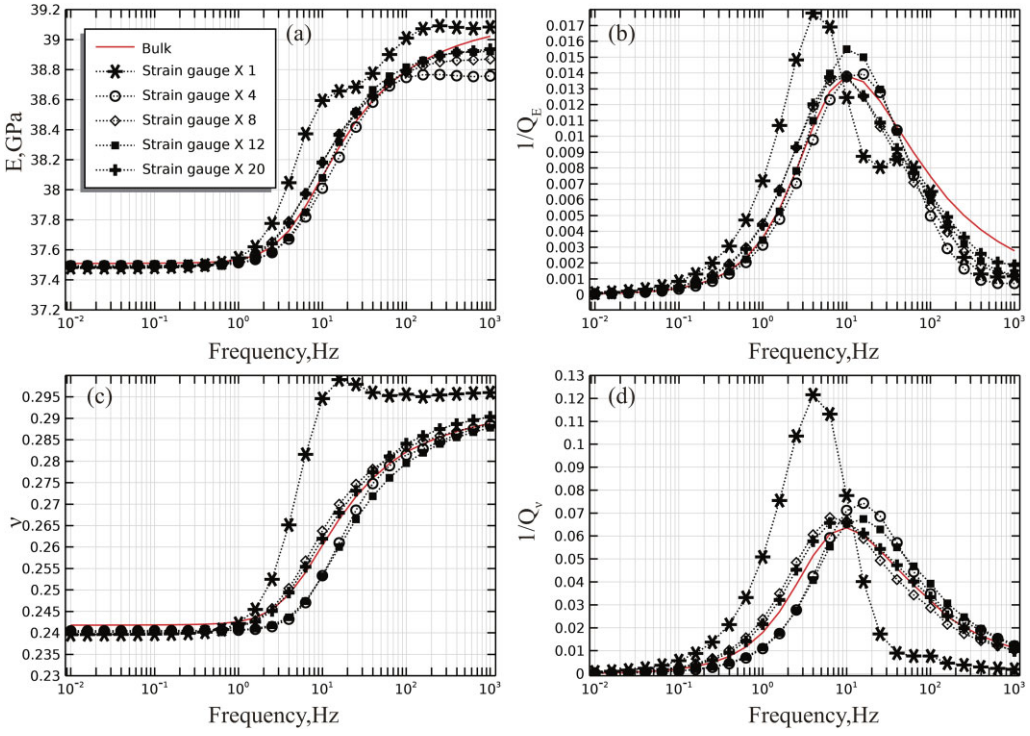

Figure 9. The local responses versus the number of strain gauges. The red line is the bulk response of the sample, and the dashed lines with different markers correspond to the local response obtained by strain gauges. (a) the Young's modulus; (b) the Young's attenuation; (c) the Poisson's ratio and (d) the Poisson's phase difference.

air patches but different spatial distributions for 10 and 30 mm correlation lengths, respectively.

Secondly, according to Monte Carlo theory, the mean of the elastic responses $\beta^n(f_m)\,(n = 1, \ldots, N_R)$ represents the statistical characteristics of the elastic response of the rock sample:

$$\beta^L(f_m,\ N_R) = \frac{1}{N_R}\sum_{n=1}^{N_R}\beta^n(f_m), \tag{16}$$

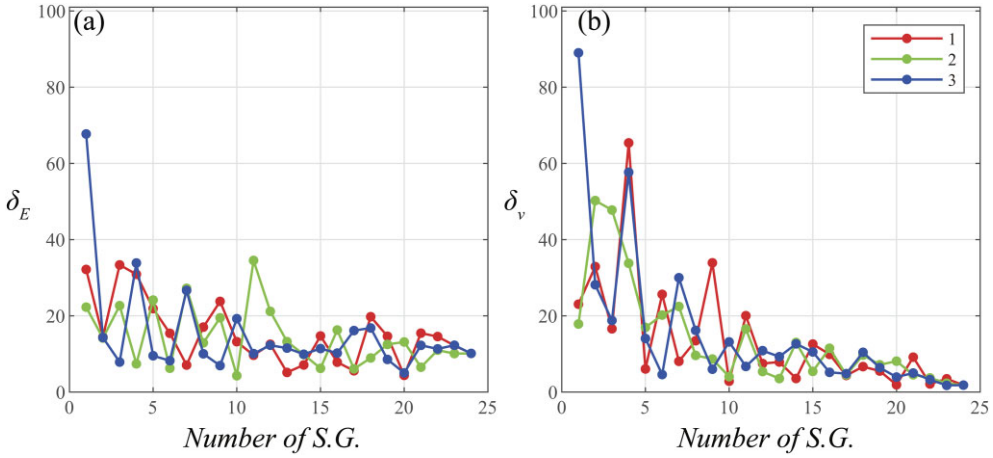

Figure 10. Evolution of relative error with respect to the number of strain gauges for both local and bulk responses. (a) Relative error for Young's modulus; (b) Relative error for Poisson's ratio. The three colours (#1–#3) represent three random selections of strain gauges. S.G. stands for strain gauge.

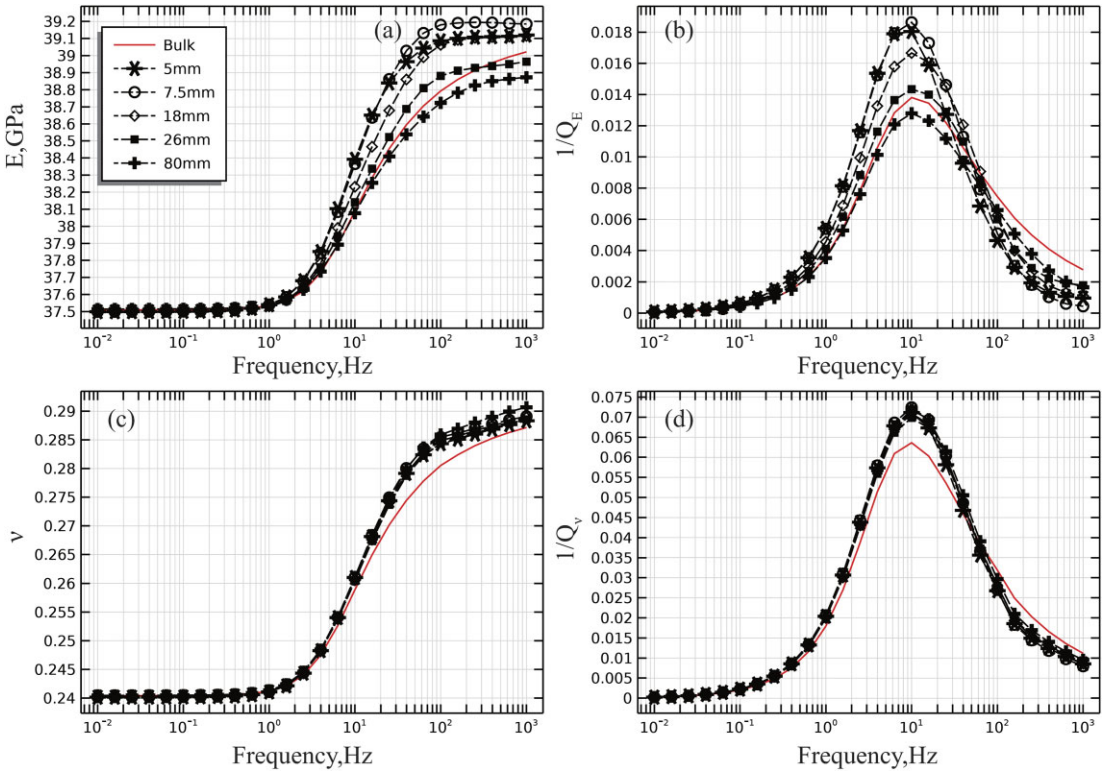

Figure 11. The calculated Young's modulus (a), Young's attenuation (b), Poisson's ratio (c) and Poisson's phase difference (d) versus the length of the strain gauges. The red line is the bulk response.

where N_R is the total number of samples. f_m $(m = 1, \ldots, N_F)$ where N_F is the total number of frequencies investigated. Taking $\beta^L(f_m, N_R)$ into eqs (13) and (14) as the local response, we can get the relative error variations with the N_R. When the $\beta^n(f_m)$ is the Young's modulus, the relative errors $\delta_E(N_R)$ for a correlation length of 3 mm, 5 mm, 1 cm and 3 cm are shown in Fig. 14.

When the correlation length is 3 mm, the relative error δ_E decreases with the increase of N_R for all three measurement scenarios: one short, four short and four long strain gauges. As the strain gauge number increases from one to four, the critical N_R decreases from 28 (blue line, Fig. 14a) to 13 (black line, Fig. 14a), and the relative error δ_E decreases from a maximum of 30 per cent (blue line, Fig. 14a) to 15 per cent (black line, Fig. 14a). In addition, the relative error δ_E above the critical N_R remains at about 1.5 per cent with the increase in the strain gauge number. On the other hand, with the increase in the strain gauge length from 5 mm (black line, Fig. 14a) to 26 mm (red line, Fig. 14a), the critical N_R decreases from 13 to 10, while the maximum relative error δ_E decreases from 15 per cent (black line, Fig. 14a) to 6 per cent (red line, Fig. 14a). Therefore, we can conclude that the increase in the strain gauge number and length can reduce the critical N_R and the overall relative error. For N_R=19 (green dashed line, Fig. 14a), the relative errors are 3.5, 1.5 and 1.5 per cent for the one short, four short and four long strain gauges, respectively. The corresponding Young's moduli (Fig. 15a) from the three cases approximate the bulk response of the cuboid, with slight deviations mainly appearing at frequencies above 30 Hz since fluid

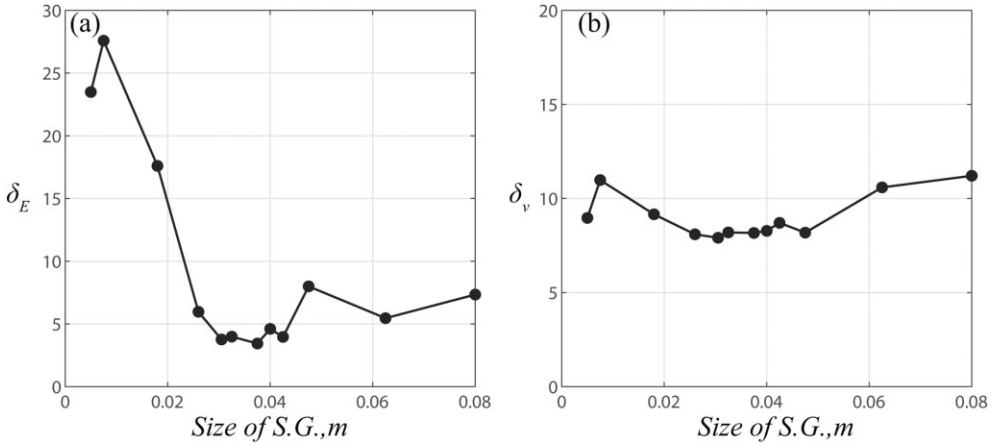

Figure 12. The relative error of the local response compared to the bulk response for gauge size in the 5–80 mm range. (a) The Young's modulus and (b) the Poisson's ratio.

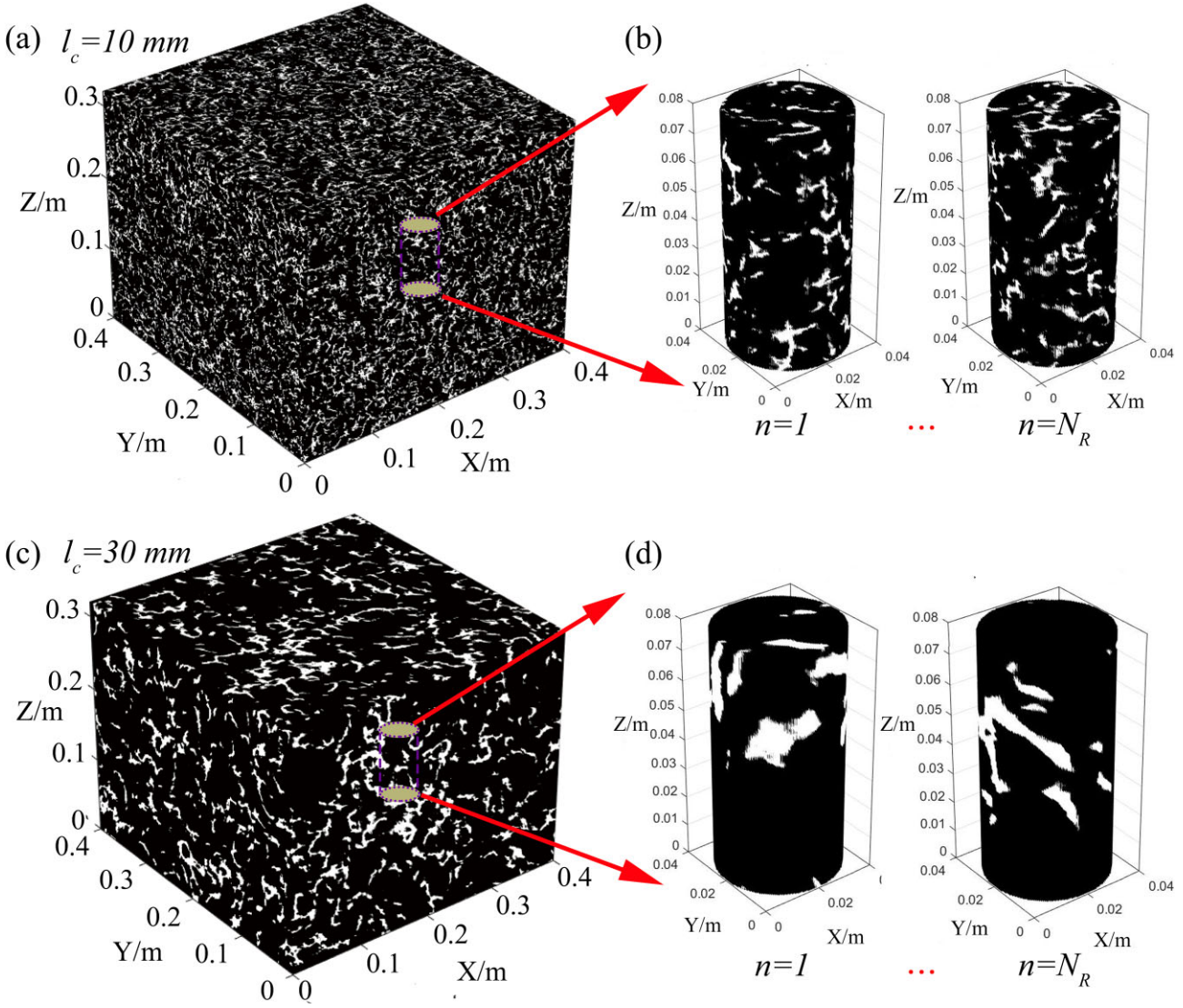

Figure 13. The reservoir cuboid has a length and width of 0.4 m and a height of 0.32 m, and its fluid distribution is characterized by the von Karman function with the Hurst exponent H of 0.8, the water saturation of 0.89 and the fractal dimension D of 3.2. (a) the correlation l_c is 10 mm; (b) N_R samples with a diameter of 0.04 m and length of 0.08 m are selected from (a) when the water saturation is 0.89; (c) the correlation length l_c is 30 mm and (d) N_R samples with a diameter of 0.04 m and length of 0.08 m are selected from (c) when the water saturation is 0.89. The black zones represent regions of full water saturation, and the white regions indicate full gas saturation.

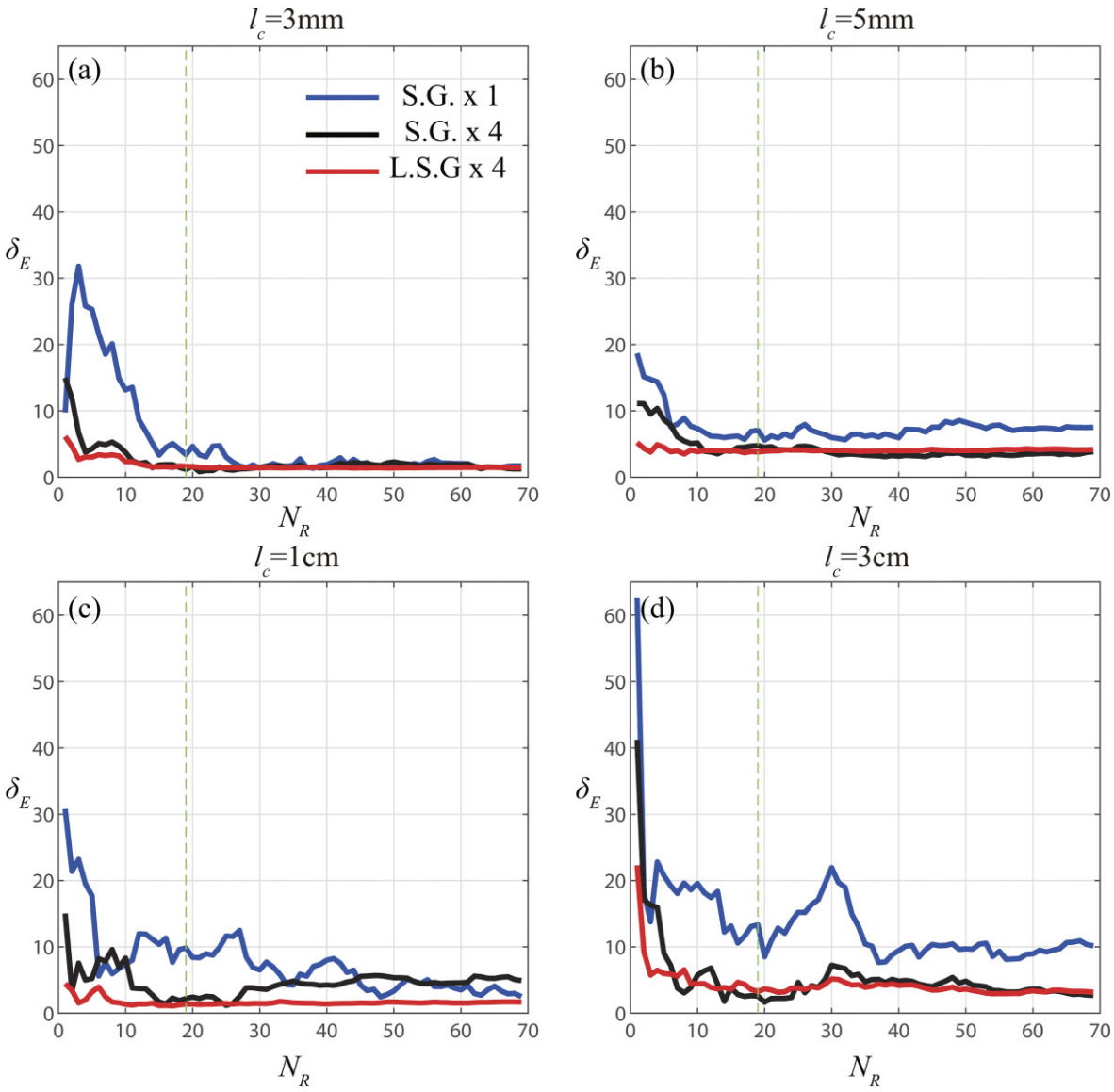

Figure 14. The relative error of Young's modulus versus the total number of the samples N_R, when the correlation length is (a) 3 mm, (b) 5 mm, (c) 1 cm and (d) 3 cm.

heterogeneity effects are more significant at high frequencies, as discussed in Section 3.1.

When the correlation length increases to 5 mm (Fig. 14b), the critical N_R remains almost consistent with that of 3 mm for the three cases. However, the relative error above the critical N_R increases from 1.5 to 6 per cent for the one-short strain gauge and from 1.5 to 4 per cent for both the four-short and four-long strain gauges. It indicates that the increase in the correlation length leads to higher relative error levels. For N_R=19, the relative errors are 7.0, 5.0 and 4.2 per cent for the one-short, four-short and four-long strain gauges, respectively. The corresponding Young's moduli from the three measurement cases are shown in Fig. 15(b). It was observed that the local responses differ from the bulk response of the cuboid for frequencies above 25 Hz, which can be attributed to the longer time required for fluid pressure equilibrium compared to 30 Hz at the correlation length of 3 mm. It is because a higher correlation length implies greater heterogeneity in fluid pressure, which leads to longer relaxation times (lower frequencies) for fluid pressure.

For the correlation length of 1 cm, the critical N_R for the one-short strain gauge, four-short and four-long strain gauges are 33, 15 and 10, respectively. In addition, the maximum relative error increased from 20 per cent (blue line, Fig. 14b) to 30 per cent (blue line, Fig. 14c) for the one-short strain gauge, and from 10 per cent (black line, Fig. 14b) to 30 per cent (black line, Fig. 14c) for the four-short strain gauges. However, there is no more variation in the maximum error for the four-long strain gauges. These results show that the increase in the correlation length leads to a higher critical N_R. In addition, the N_R for the long strain gauges is less affected compared to that of the short strain gauges. Taking N_R=19 (green line in Fig. 14c), the corresponding Young's moduli for the three cases are shown in Fig. 15(c). Again, as we expect, the frequency at which the local and bulk responses start to deviate decreases from 25 to 1 Hz due to the more heterogeneous fluid distribution.

For the correlation length of 3 cm, the critical N_R for the one-short strain gauge, four-short and four-long strain gauges are 39, 35 and 15, respectively. They are larger than the N_R (33, 15 and

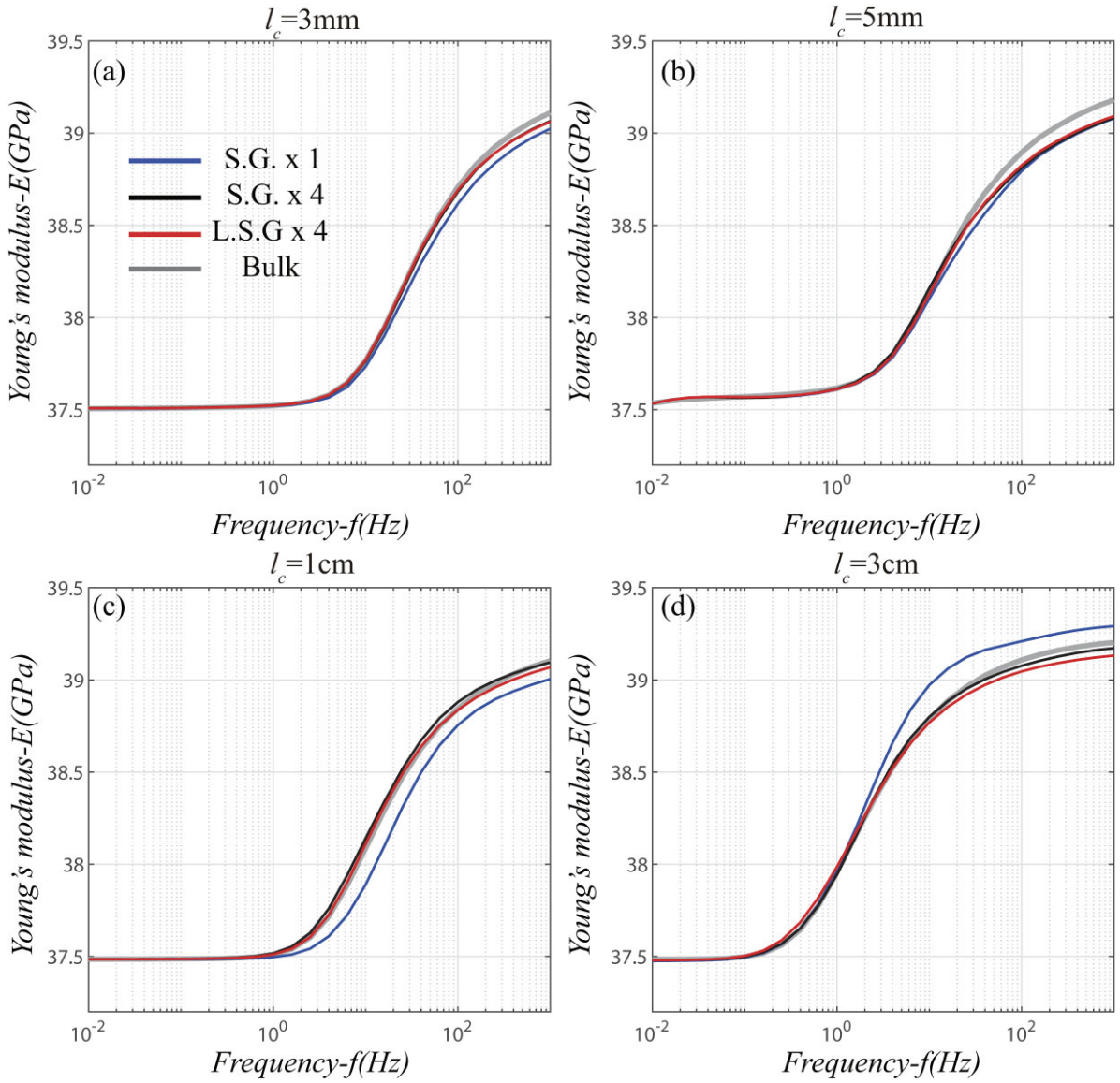

Figure 15. The Young's modulus from the one-short (blue), four-short (black) and four-long (red) strain gauges when N_R is 19. The grey line is the bulk response from the reservoir cuboid. The correlation lengths for the fluid distribution are (a) 1 mm, (b) 5 mm, (c) 1 cm and (d) 3 cm.

10) at the correlation length of 1 cm. In addition, the maximum relative error increases from 30 per cent (blue line, Fig. 14c) to 60 per cent (blue line, Fig. 14d) for the one-short strain gauge, from 15 per cent (black line, Fig. 14c) to 42 per cent (black line, Fig. 14d) for the four-short strain gauges and from 5 per cent (red line, Fig. 14c) to 21 per cent (red line in Fig. 14d) for the four-long strain gauges. These variations show that the long strain gauges will also fail to get an approximate bulk response as the correlation length increases. Taking $N_R = 19$ (green line in Fig. 11c), the corresponding local responses of Young's modulus are shown in Fig. 15(d). As expected, the frequency at which the local and bulk responses deviate decreases from 1 to 0.6 Hz.

Overall, increasing the total number of samples (N_R) tends to decrease the relative error between local measurements and the bulk response of the reservoir. However, the size and number of strain gauges also play a role in determining the critical N_R. Specifically, as the size and number of strain gauges increase, the critical N_R tends to decrease. It means that for a given level of fluid heterogeneity, more strain gauges or larger strain gauges are needed to achieve a certain level of accuracy.

4.2 The effect of the heterogeneity

According to the above analysis, the error between the local measurement and the bulk response of the cuboid depends on the fluid heterogeneity. However, increasing the size of the strain gauge can reduce this effect. Thus, it is important to determine the optimal strain gauge size that can be used to accurately characterize the elastic response of natural rock with an acceptable relative error.

We defined a ratio $\frac{l_{S.G.}}{l_c}$ to address the issue, where $l_{S.G.}$ is the length of the strain gauge and l_c is correlation length, respectively. Four bi-axial strain gauges at mid-height of the sample are used to do the investigation. It is a standard procedure in the forced-oscillation experiment. Fig. 16 shows the relative error of the Young's modulus versus the ratio $\frac{l_{S.G.}}{l_c}$.

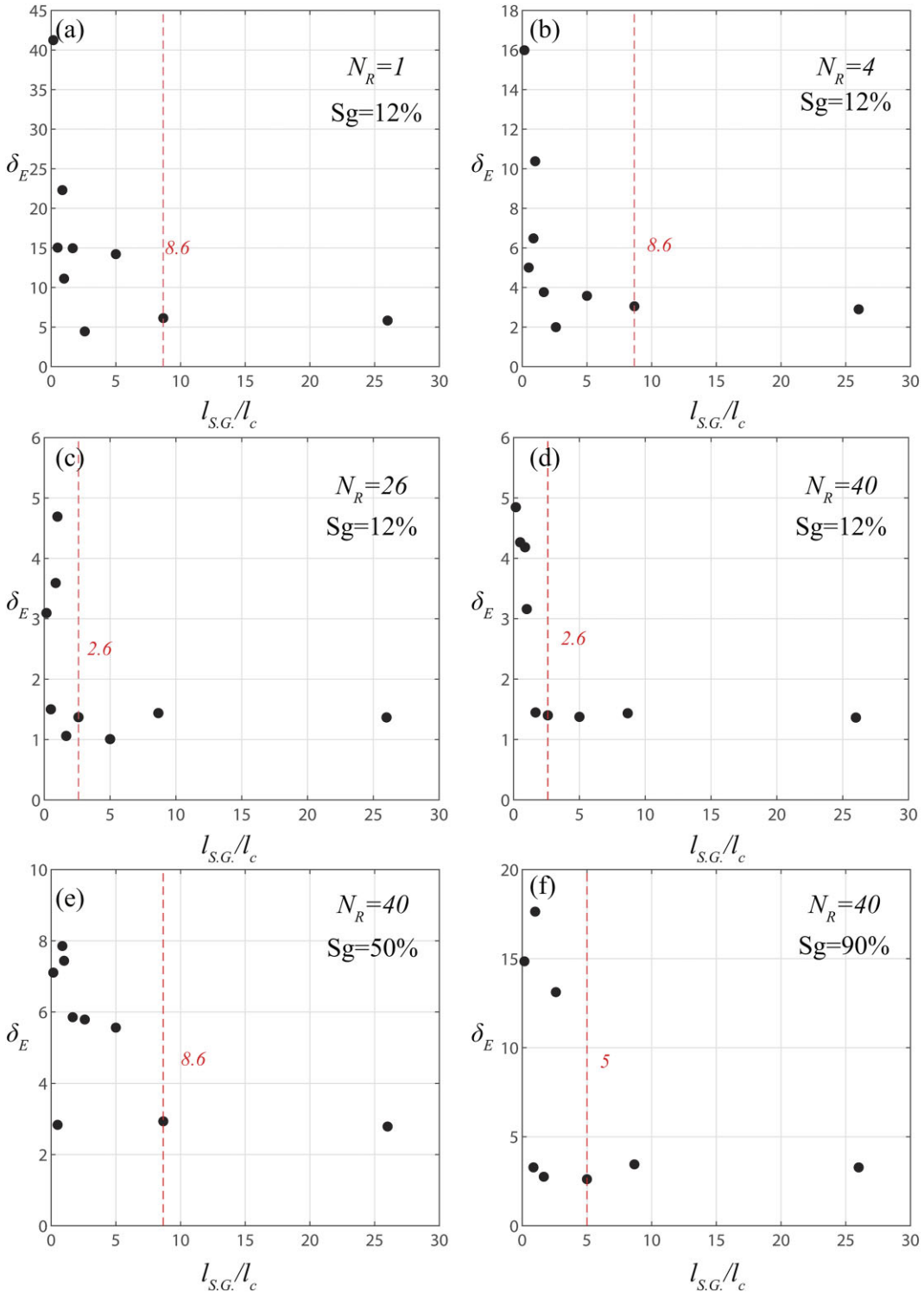

Figure 16. The relative error of Young's modulus versus the ratio of strain gauge length to the correlation length. (a) N_R = 1, Sg = 12 per cent; (b) N_R = 4, Sg = 12 per cent; (c) N_R=26, Sg = 12 per cent; (d) N_R = 40, Sg = 12 per cent; (e) N_R=40, Sg = 50 per cent; (f) N_R=40, Sg = 90 per cent. N_R is the total number of the samples, and Sg is the air saturation.

For the air saturation of 12 per cent and N_R=1 (Fig. 16a), the relative error drops from 40 to 6 per cent as the ratio $\frac{l_{S.G.}}{l_c}$ increases from 0.16 to 8.6, and remains at 6 per cent as the ratio $\frac{l_{S.G.}}{l_c}$ increases from 8.6 to 26. It means that the strain gauge size should be at least 8.6 times the correlation length to obtain the lowest relative error for one sample. As N_R increases from 1 to 4 (Fig. 16b), the maximum relative error decreases from 40 to 16 per cent, and the minimum relative error decreases from 6 to 2.5 per cent. However, the critical $\frac{l_{S.G.}}{l_c}$ is still 8.6. As the N_R increases from 4 to 26 (Fig. 16c), the maximum relative error decreases from 16 to 4.8 per cent, and the minimum relative error decrease from 2.5 to 1.5 per cent. In addition, the critical ratio of $\frac{l_{S.G.}}{l_c}$ decreases from 8.6 to 2.6. Therefore,

the increase in the N_R can reduce both the relative error and the critical ratio $\frac{l_{S.G.}}{l_c}$. As the N_R increases from 26 to 40 (Fig. 16d), there is no more change for both the relative error and critical ratio $\frac{l_{S.G.}}{l_c}$. It means there is a critical N_R, above which the relative error and critical ratio are independent of the N_R.

As the air saturation increases from 12 to 50 per cent (Fig. 16e) and the N_R is 40, the maximum relative error increases from 4.8 to 7.8 per cent, and the minimum relative error increases from 1.5 to 2.5 per cent. In addition, the critical $\frac{l_{S.G.}}{l_c}$ increases from 2.6 to 8.6. As the air saturation further increases from 50 to 90 per cent (Fig. 16f), the maximum relative error increases from 7.8 to 17.5 per cent, and the minimum relative error increases from 2.5 to 4.8 per cent. However, the critical ratio decreases slightly, from 8.6 to 5.0. We can thus conclude that fluid saturation can affect the magnitude of the relative error and the critical ratio $\frac{l_{S.G.}}{l_c}$. It is worth noting that although the relative error increases as the air saturation increases, the absolute error could decrease because the elastic response at a high air saturation is less dispersive than that at a low air saturation.

In summary, our study suggests that using strain gauges with a size 8.6 times larger than the correlation length can reduce the relative error to as low as 6 per cent for one sample with four strain gauges. Furthermore, increasing the total number of tested samples can further lower the critical ratio and relative error. Fluid saturation also affects the critical ratio, although not to the same extent as the total number of samples. These findings can help guide laboratory measurements for investigating reservoir seismic dispersion and attenuation. However, our study focused only on fluid heterogeneities and did not consider rock matrix heterogeneities such as fractures (Guo *et al*. 2018, Gallagher *et al*. 2022) and dual-porosity medium (Ba *et al*., 2015), which could complicate the issue. Therefore, future research should aim to address these challenges.

5 CONCLUSIONS

In this study, we conducted numerical simulations to investigate the impact of fluid-spatial heterogeneity on the local measurement of attenuation and elastic dispersion of partially saturated rocks. Our results revealed a significant difference between the local measurement and bulk response for biphasic saturated samples, which depends on the location of the strain gauge due to its limited ability to probe a small portion of the sample's surface. Both horizontal and vertical strain gauge locations considerably influence the local response of various elastic parameters, such as the Young's modulus, the Young's attenuation, the Poisson's ratio, and the Poisson's phase difference. However, increasing the number and size of strain gauges can approximate the bulk response and reduce the error between the local and global responses. We identified critical values for the strain gauge number and size, beyond which the error remains stable, such as a critical strain gauge number of 6–8 and a critical strain size of around 26 mm for quasi-fractal fluid distribution with a correlation length of 1 cm. Simultaneously increasing the number and size of strain gauges reduce the differences between local and bulk responses compared to using either method alone.

To further examine the error between the laboratory's local response and the reservoir's bulk response, we utilized the Monte Carlo procedure. Our findings indicate that increasing the number of test samples reduces the relative error between the laboratory's local measurements and the bulk response of the reservoir. The critical number of test samples depends on the size and number of the strain gauge, and increasing the size and number of strain gauges can reduce the critical number of test samples. Fluid heterogeneity also affects the critical number of the test sample, with an increase in fluid heterogeneity leading to a higher critical number of test samples for the same strain gauge number and size. To quantitatively assess the effect of the heterogeneous fluid distribution, we conducted an analysis of the relative error versus the ratio of the strain gauge length to the correlation length. Our analysis indicates that the relative error can be as low as 6 per cent for the local measurement of four strain gauges when the ratio of the strain gauge length to the correlation length is 8.6. Furthermore, the relative error can decrease further to 1.5 per cent with an increase in the total number of test samples. The critical ratio is influenced by fluid saturation but not as much as the total number of tested samples.

By implementing these findings, we can better understand the impact of fluid-spatial heterogeneity on the local measurement of attenuation and elastic dispersion of partially saturated rocks, which has implications for oil and gas exploration industries. Additionally, our findings provide valuable guidance for rock physicists investigating frequency-dependent effects in biphasic saturated rock using the forced oscillation apparatus, enabling them to reduce local measurement errors.

CODE AVAILABILITY STATEMENT

COMSOL multiphysics is used for meshing and finite element solving. The codes related to the figures in the main text are available by contacting the author at 'kang2008ping2008@163.com'.

ACKNOWLEDGMENTS

This work is supported by the National Natural Science Foundation of China (42104111, 42274142, 41930425, 41774143, 41804104) and also supported by Open Fund (WX-KFJJ-2022-08) of SINOPEC Key Laboratory of Geophysics, and State Key Laboratory of Petroleum Resources and Prospecting, China University of Petroleum and Xuzhou Science and Technology Bureau Young Talents Project (No. KC22018).

CONFLICT OF INTEREST

The authors declare that they have no conflict of interest.

REFERENCES

Atalla, N., Panneton, R. & Debergue, P. 1998. A mixed displacement-pressure formulation for poroelastic materials. *J. acoust. Soc. Am.,* **104**(3), 1444–1452.

Ba, J., Carcione, J. M. & Sun, W. 2015. Seismic attenuation due to heterogeneities of rock fabric and fluid distribution. *Geophys. J. Int.,* **202**(3), 1843–1847.

Batzle, M. L., Han, D.-H. & Hofmann, R. 2006. Fluid mobility and frequency-dependent seismic velocity—direct measurements. *Geophysics,* **71**(1), N1–N9.

Biot, M. A. 1941. General theory of three-dimensional consolidation. *J. appl. Phys.,* **12**(2), 155–164.

Biot, M.A. 1956a. Theory of propagation of elastic waves in a fluid-saturated porous solid. I. Low-frequency range. *J. acoust. Soc. Am.,* **28,** 168–178.

Biot, M. A. 1956b. Theory of propagation of elastic waves in a fluid-saturated porous solid. II. Higher frequency range. *J. acoust. Soc. Am.,* **28**(2), 179–191.

Biot, M. A. 1962. Mechanics of deformation and acoustic propagation in porous media. *J. appl. Phys.,* **33**(4), 1482–1498.

Biot, M. A. & Willis, D. G. 1957. The elastic coefficients of the theory of consolidation. *ASME. J. Appl. Mech,* **24**(4): 594–601.

Borgomano, J. V. M., Gallagher, A., Sun, C. & Fortin, J. 2020. An apparatus to measure elastic dispersion and attenuation using hydrostatic- and axial-stress oscillations under undrained conditions. *Rev. Sci. Instrum.,* **91**(3), 034502.

Born, W. T. 1941. The attenuation constant of earth materials. *Geophysics,* **6**(2), 132–148.

Cadoret, T., Mavko, G. & Zinszner, B. 1998. Fluid distribution effect on sonic attenuation in partially saturated limestones. *Geophysics,* **63**(1), 154–160.

Chapman, S. & Quintal, B. 2018. Numerical assessment of local versus bulk strain measurements to quantify seismic attenuation in partially saturated rocks, in *Proceedings of the SEG Technical Program Expanded Abstracts 2018,* Vols 1–0, pp. 3547–3551, Society of Exploration Geophysicists.

Chapman, S., Borgomano, J. V., Yin, H., Fortin, J. & Quintal, B. 2019. Forced oscillation measurements of seismic wave attenuation and stiffness moduli dispersion in glycerine-saturated Berea sandstone. *Geophys. Prospect.,* **67**(4), 956–968.

Chapman, S., Borgomano, J. V. M., Quintal, B., Benson, S. M. & Fortin, J. 2021. Seismic wave attenuation and dispersion due to partial fluid saturation: direct measurements and numerical simulations based on X-ray CT. *J. geophys. Res.,* **126**(4), doi:10.1029/2021JB021643.

Dutta, N. C. & Ode, H. 1979. Attenuation and dispersion of compressional waves in fluid-filled porous rocks with partial gas saturation (White model). Part II: results. *Geophysics,* **44**(11), 1789–1805.

Gallagher, A., Fortin, J. & Borgomano, J. 2022. Seismic dispersion and attenuation in fractured fluid-saturated porous rocks: an experimental study with an analytic and computational comparison. *Rock Mech. Rock Eng.,* **55**(7), 4423–4440.

Gordon, R. B. & Davis, L. A. 2012. Velocity and attenuation of seismic waves in imperfectly elastic rock. *J. geophys. Res.,* **73**(12), 3917–3935.

Gurevich, B., Brajanovski, M., Galvin, R. J., Müller, T. M. & Toms-Stewart, J. 2009. P-wave dispersion and attenuation in fractured and porous reservoirs – poroelasticity approach. *Geophys. Prospect.,* **57**(2), 225–237.

Guo, J., Germán Rubino, J., Barbosa, N. D., Glubokovskikh, S. & Gurevich, B. 2018. Seismic dispersion and attenuation in saturated porous rocks with aligned fractures of finite thickness: theory and numerical simulations — Part 2: frequency-dependent anisotropy. *GEOPHYSICS,* **83**(1), WA63–WA71.

Guo, J., Gurevich, B. & Chen, X. 2022a. Dynamic SV-wave signatures of fluid-saturated porous rocks containing intersecting fractures. *J. geophys. Res.,* **127**(8), e2022JB024745.

Guo, J., Zhao, L., Chen, X., Yang, Z., Li, H. & Liu, C. 2022b. Theoretical modelling of seismic dispersion, attenuation and frequency-dependent anisotropy in a fluid-saturated porous rock with intersecting fractures. *Geophys. J. Int.,* **230**(1), 580–606.

Harris, J., Quan, Y. & Xu, C. 2005. Differential acoustical resonance spectroscopy: an experimental method for estimating acoustic attenuation of porous media, in *Proceedings of the SEG Technical Program Expanded Abstracts 2005,* Vols 1–0, pp. 1569–1572, Society of Exploration Geophysicists.

Helle, H. B., Pham, N. H. & Carcione, J. M. 2003. Velocity and attenuation in partially saturated rocks: poroelastic numerical experiments: velocity and attenuation for patchy saturation. *Geophys. Prospect.,* **51**(6), 551–566.

Hill, R. 1963. Elastic properties of reinforced solids: some theoretical principles. *J. Mech. Phys. Solids,* **11**(5), 357–372.

Klimeš, L. 2002. Correlation functions of random media. *Pure appl. Geophys.,* **159,** 1811–1831.

Kumar, G. 2003. Fluid effects on attenuation and dispersion of elastic waves, *Master thesis,* Colorado School of Mines, Golden, CO, USA.

Li, H., Lin, J., Gao, J., He, Y., Han, D. & Zhao, L. 2020. Precision analysis of forced-oscillation device: numerical modelling and experimental investigations. *J. Geophys. Eng.,* **17**(6), 980–992.

Masson, Y. J. & Pride, S. R. 2007. Poroelastic finite difference modeling of seismic attenuation and dispersion due to mesoscopic-scale heterogeneity. *J. geophys. Res.,* **112**(B3), doi:10.1029/2006JB004592.

Mavko, G., Mukerji, T. & Dvorkin, J. 2009. *The Rock Physics Handbook: Tools for Seismic Analysis of Porous Media,* Cambridge Univ. Press.

McCann, C. & Sothcott, J. 2009. Sonic to ultrasonic Q of sandstones and limestones: laboratory measurements at in situ pressures. *Geophysics,* **74**(2), WA93–WA101.

Mikhaltsevitch, V., Lebedev, M. & Gurevich, B. 2011. A low-frequency apparatus for characterizing the mechanical properties of rocks, in *Presented at the 73rd EAGE Conference and Exhibition incorporating SPE EUROPEC 2011,* May 2011, cp-238-00537, European Association of Geoscientists & Engineers.

Mikhaltsevitch, V., Lebedev, M. & Gurevich, B. 2014. A laboratory study of elastic and anelastic properties of Savonnieres Limestone (Vol. 2014, pp. 1–5), in *Presented at the 76th EAGE Conference and Exhibition 2014,* Amsterdam, Netherlands, European Association of Geoscientists & Engineers.

Mikhaltsevitch, V., Lebedev, M. & Gurevich, B. 2015. A laboratory study of attenuation and dispersion effects in glycerol-saturated Berea sandstone at seismic frequencies, in *SEG Technical Program Expanded Abstracts 2015,* pp. 3085–3089, Society of Exploration Geophysicists.

Müller, T. M., Toms-Stewart, J. & Wenzlau, F. 2008. Velocity-saturation relation for partially saturated rocks with fractal pore fluid distribution. *Geophys. Res. Lett.,* **35**(9), doi:10.1029/2007GL033074.

Müller, T. M., Gurevich, B. & Lebedev, M. 2010. Seismic wave attenuation and dispersion resulting from wave-induced flow in porous rocks: a review. *Geophysics,* **75**(5), 75A147–75A164.

Pimienta, L., Fortin, J. & Guéguen, Y. 2015. Bulk modulus dispersion and attenuation in sandstones. *Geophysics,* **80**(2), D111–D127.

Pimienta, L., Borgomano, J. V. M., Fortin, J. & Guéguen, Y. 2016. Modelling the drained/undrained transition: effect of the measuring method and the boundary conditions: Modelling drained/undrained transition. *Geophys. Prospect.,* **64**(4), 1098–1111.

Pimienta, L., Fortin, J. & Guéguen, Y., 2017. New method for measuring compressibility and poroelasticity coefficients in porous and permeable rocks, *J. geophys. Res.,* **122,** 2670–2689.

Quintal, B., Frehner, M., Madonna, C., Tisato, N., Kuteynikova, M. & Saenger, E. H. 2011. Integrated numerical and laboratory rock physics applied to seismic characterization of reservoir rocks. *Leading Edge,* **30**(12), 1360–1367.

Ravalec, M. L., Noetinger, B. & Hu, L. Y. 2000. The FFT moving average (FFT-MA) generator: an efficient numerical method for generating and conditioning Gaussian simulations, *Math. Geol.,* **32,** 701–723.

Rubino, J. G., Ravazzoli, C. L. & Santos, J. E. 2009. Equivalent viscoelastic solids for heterogeneous fluid-saturated porous rocks. *Geophysics,* **74**(1), N1–N13.

Rubino, J. G., Caspari, E., Müller, T. M., Milani, M., Barbosa, N. D. & Holliger, K. 2016. Numerical upscaling in 2-D heterogeneous poroelastic rocks: anisotropic attenuation and dispersion of seismic waves. *J. geophys. Res.,* **121**(9), 6698–6721.

Santos, J. E., Ravazzoli, C. L., Gauzellino, P. M. & Carcione, J. M. 2005. Numerical simulation of ultrasonic waves in reservoir rocks with patchy saturation and fractal petrophysical properties. *Comput. Geosci.,* **9**(1), 1–27.

Skempton, A. W. 1954. The pore-pressure coefficients A and B. *Géotechnique,* **4**(4), 143–147.

Spencer, J. W. 1981. Stress relaxations at low frequencies in fluid-saturated rocks: attenuation and modulus dispersion. *J. geophys. Res.,* **86**(B3), 1803–1812.

Spencer, J. W. & Shine, J. 2016. Seismic wave attenuation and modulus dispersion in sandstones. *Geophysics,* **81**(3), D211–D231.

Subramaniyan, S., Quintal, B., Tisato, N., Saenger, E. H. & Madonna, C. 2014. An overview of laboratory apparatuses to measure seismic attenuation in reservoir rocks: apparatuses to measure seismic attenuation. *Geophys. Prospect.,* **62**(6), 1211–1223.

Sun, C., Tang, G., Zhao, J., Zhao, L. & Wang, S. 2018. An enhanced broad-frequency-band apparatus for dynamic measurement of elastic moduli and Poisson's ratio of rock samples. *Rev. Sci. Instrum.,* **89**(6), doi:10.1063/1.5018152.

Sun, C., Tang, G., Fortin, J., Borgomano, J. V. M. & Wang, S. 2020. Dispersion and attenuation of elastic wave velocities: impact of microstructure heterogeneity and local measurements. *J. geophys. Res.,* **125**(12), e2020JB020132.

Sun, C., Fortin, J., Borgomano, J. V. M., Wang, S., Tang, G., Bultreys, T. & Cnudde, V. 2022. Influence of fluid distribution on seismic dispersion and attenuation in partially saturated limestone. *J. geophys. Res.,* **127**(5), doi:10.1029/2021JB023867.

Teja, A. S. & Rice, P. 1981. Generalized corresponding states method for the viscosities of liquid mixtures. *Indust. Eng. Chem. Fundament.,* **20**(1), 77–81.

Tisato, N. & Madonna, C. 2012. Attenuation at low seismic frequencies in partially saturated rocks: measurements and description of a new apparatus. *J. appl. Geophys.,* **86,** 44–53.

Toms-Stewart, J., Müller, T. M., Gurevich, B. & Paterson, L. 2009. Statistical characterization of gas-patch distributions in partially saturated rocks. *Geophysics,* **74**(2), WA51–WA64.

Wang, H. 2000. *Theory of Linear Poroelasticity with Applications to Geomechanics and Hydrogeology,* Vol. 2, Princeton Univ. Press.

Wang, S., Zhao, J., Li, Z., Harris, J. M. & Quan, Y. 2012. Differential acoustic resonance spectroscopy for the acoustic measurement of small and irregular samples in the low frequency range. *J. geophys. Res.,* **117**(B6), doi:10.1029/2011JB008808.

Winkler, K. & Nur, A. 1979. Pore fluids and seismic attenuation in rocks. *Geophys. Res. Lett.,* **6**(1), 1–4.

Yin, H., Zhao, J., Tang, G., Zhao, L., Ma, X. & Wang, S. 2017. Pressure and fluid effect on frequency-dependent elastic moduli in fully saturated tight sandstone. *J. geophys. Res.,* **122**(11), 8925–8942.

Yin, H., Borgomano, J. V. M., Wang, S., Tiennot, M., Fortin, J. & Guéguen, Y. 2019. Fluid substitution and shear weakening in clay-bearing sandstone at seismic frequencies. *J. geophys. Res.,***124,** 1254–1272.

Zhao, J., Tang, G., Deng, J., Tong, X. & Wang, S. 2013. Determination of rock acoustic properties at low frequency: a differential acoustical resonance spectroscopy device and its estimation technique. *Geophys. Res. Lett.,* **40**(12), 2975–2982.

Zhao, L., *et al.* 2019. Laboratory study of oil saturation and oil/water substitution effects on a sandstone's modulus dispersion and attenuation. *Explor. Geophys.,* **50**(3), 324–335.

Zhao, L., Tang, G., Sun, C., Zhao, J. & Wang, S. 2021. Dual attenuation peaks revealing mesoscopic and microscopic fluid flow in partially oil-saturated Fontainebleau sandstones. *Geophys. J. Int.,* **224**(3), 1670–1683.